HHS Public Access

Author manuscript

Nature. Author manuscript; available in PMC 2016 April 23.

Published in final edited form as:

Nature. 2016 February 25; 530(7591): 441–446. doi:10.1038/nature16998.

The dynamic N^1-methyladenosine methylome in eukaryotic messenger RNA

Dan Dominissini[1,2,*], **Sigrid Nachtergaele**[1,2,*], **Sharon Moshitch-Moshkovitz**[3,*], **Eyal Peer**[3,4], **Nitzan Kol**[3], **Moshe Shay Ben-Haim**[3,4], **Qing Dai**[1,2], **Ayelet Di Segni**[3], **Mali Salmon-Divon**[3], **Wesley C. Clark**[6], **Guanqun Zheng**[6], **Tao Pan**[6], **Oz Solomon**[3,5], **Eran Eyal**[3], **Vera Hershkovitz**[3], **Dali Han**[1,2], **Louis C. Doré**[1,2], **Ninette Amariglio**[3,5], **Gideon Rechavi**[3,4], and **Chuan He**[1,2,6]

[1]Department of Chemistry and Institute for Biophysical Dynamics, The University of Chicago, 929 East 57th Street, Chicago, Illinois 60637, USA

[2]Howard Hughes Medical Institute, The University of Chicago, 929 East 57th Street, Chicago, Illinois 60637, USA

[3]Cancer Research Center, Chaim Sheba Medical Center, Tel Hashomer 52621, Israel

[4]Sackler School of Medicine, Tel Aviv University, Tel Aviv 69978, Israel

[5]The Mina and Everard Goodman Faculty of Life Sciences, Bar-Ilan University, Ramat Gan 52900, Israel

[6]Department of Biochemistry and Molecular Biology, The University of Chicago, 929 East 57th Street, Chicago, Illinois 60637, USA

Abstract

Gene expression can be regulated post-transcriptionally through dynamic and reversible RNA modifications. A recent noteworthy example is N^6-methyladenosine (m^6A), which affects messenger RNA (mRNA) localization, stability, translation and splicing. Here we report on a new mRNA modification, N^1-methyladenosine (m^1A), that occurs on thousands of different gene transcripts in eukaryotic cells, from yeast to mammals, at an estimated average transcript

Correspondence and requests for materials should be addressed to D.D. (dandominissini@gmail.com), G.R. (gidi.rechavi@sheba.health.gov.il) or C.H. (chuanhe@uchicago.edu).

*These authors contributed equally to this work.

Online Content Methods, along with any additional Extended Data display items and Source Data, are available in the online version of the paper; references unique to these sections appear only in the online paper.

Supplementary Information is available in the online version of the paper.

Author Contributions D.D. and C.H. conceived the idea. D.D. designed the experiments and analyses, and developed the method. D.D., S.N., and S.M.-M. performed experiments. A.D.S. performed PARS structural mapping. V.H., Q.D., and G.Z. helped with experiments. Q.D. synthesized deuterated standards. D.D., S.M.-M., S.N., M.S.B.-H., E.P., N.K., M.S.-D., O.S., E.E., W.C.C. and D.H. performed analyses and interpreted findings. D.D., S.M.-M., S.N. and C.H. wrote the manuscript with input from M.S.B.-H., E.P., L.C.D., W.C.C., G.Z., T.P., N.A. and G.R.

Data have been deposited in the NCBI Gene Expression Omnibus (GEO) and are accessible through GEO series accession number GSE70485.

The authors declare no competing financial interests.

Readers are welcome to comment on the online version of the paper.

stoichiometry of 20% in humans. Employing newly developed sequencing approaches, we show that m^{1}A is enriched around the start codon upstream of the first splice site: it preferentially decorates more structured regions around canonical and alternative translation initiation sites, is dynamic in response to physiological conditions, and correlates positively with protein production. These unique features are highly conserved in mouse and human cells, strongly indicating a functional role for m^{1}A in promoting translation of methylated mRNA.

Four decades after it was first observed as an abundant constituent of the eukaryotic transcriptome, m^{6}A has only recently been revealed to broadly affect mRNA metabolism[1,2]. Consequently, a broader notion has emerged that dynamic chemical modifications of mRNA, now also encompassing pseudouridine (Ψ)[3–5] and 5-methylcytosine[6,7], have vital roles in post-transcriptional gene regulation. With the epitranscriptome, as these modifications are now known, RNA joins both DNA and proteins in being subject to dynamic and reversible chemical control[8,9]. Unlike the latter two, however, the functions of RNA chemical adducts are only now being determined. It is likely that the complement of mRNA modifications, at present much smaller than that found on transfer RNA (tRNA) and ribosomal RNA (rRNA)[10], is far from complete.

Transcriptome-wide mapping of m¹A

m^{1}A was identified in total RNA from several species decades ago[11,12]. It was later characterized in tRNA[13] and rRNA[14] where it has a major influence on structure and function, owing to the presence of both a methyl adduct and a positive charge under physiological conditions[15]. Since m^{1}A can rearrange to m^{6}A under alkaline conditions (Dimroth rearrangement)[16], its signature in mRNA might be erased by the purification and measurement process, simultaneously introducing noise in m^{6}A measurements (Fig. 1a and Extended Data Fig. 1a), as earlier attempts to survey mRNA base modifications acknowledged[17]. To determine whether m^{1}A is present in mRNA and to quantify it, we performed quantitative mass spectrometry (LC-MS/MS) of pure mRNA preparations under controlled conditions (Supplementary Note 1, Extended Data Fig. 1b–d) and obtained m^{1}A/A molar ratios in several human and mouse cell lines and tissues, both normal and cancerous. Our results unequivocally show that m^{1}A is present in pure mammalian mRNA, at m^{1}A/A ratios ranging from approximately 0.015% to 0.054% in cell lines and up to 0.16% in tissues (Figs 1b, 5d and Extended Data Fig. 1e). Metabolic labelling of cells with deuterated methionine (d_3-Met) results in detection of d_3-m1A in mRNA, suggesting that *S*-adenosyl-methionine (SAM) is the methyl donor (Extended Data Fig. 1f). Although these ratios are smaller than the m^{6}A/A and Ψ/U ratios in the same samples (Fig. 1b), the absolute and fractional levels of m^{1}A in mRNA (see stoichiometry below) are sufficiently high to exhibit potential regulatory functions of selectively methylated transcripts.

We adapted an antibody-based approach, methylated RNA immunoprecipitation sequencing (MeRIP-seq), termed here m^{1}A-seq, for transcriptome-wide localization of m^{1}A sites and coupled it to an orthogonal chemical method based on Dimroth rearrangement to obtain high-resolution m^{1}A maps (Supplementary Notes 2, 3; Fig. 1c–e and Extended Data Fig. 1g–m). We applied m^{1}A-seq to polyA$^+$ RNA from HeLa cells in two replicates and

determined the methylated positions (m^1A peaks) using the MACS peak-calling algorithm[18]. We identified 7,154 peaks (fold change (FC) ≥2, false discovery rate (FDR) ≤5%) in 4,151 coding and 63 non-coding adequately expressed (that is, above the 1st quartile of expressed genes) gene transcripts that occurred in both replicates (Fig. 2a, Supplementary Tables 1, 4). On average, each methylated gene carries 1.4 peaks, with most of these genes (over 70%) methylated only once (Fig. 2b). In a conservative estimate, 35% of adequately expressed genes are methylated, attesting to the breadth of the phenomenon. Of note, non-coding genes are significantly underrepresented among methylated genes ($P = 1 \times 10^{-140}$, hypergeometric test). Methylated genes constitute a progressively larger fraction of genes as expression increases (Fig. 2c), and are significantly enriched in several gene ontology terms related to translation and RNA processing (Extended Data Fig. 2a, b).

As most methylated transcripts harbour a single m^1A, methylation stoichiometry can be estimated based on the change in transcript levels following immunodepletion. We used microarrays to determine relative transcript abundance in HepG2 RNA before and after depletion m^6A. Methyl groups ($-CH_3$) are in red and the positive charge (+) on with anti-m^1A antibody, and found that the average methylation level in single m^1A-containing genes is ~20% (Fig. 2e, Extended Data Fig. 2c, Supplementary Table 7). The presence of m^1A in a substantial fraction of mRNA transcripts suggests a potentially sizeable effect on mRNA metabolism.

m¹A associates with translation initiation sites and the first splice site

We found that m^1A peaks appear in all segments of transcripts—5′ untranslated region (UTR), coding sequence (CDS) and 3′ UTR—but are markedly under-represented in the latter (~fivefold depletion relative to chance, $P < 1 \times 10^{-200}$, hypergeometric test, Fig. 2d). m^1A-seq of two additional cell lines in replicates, HepG2 and HEK293, produced similar distribution patterns (Fig. 2b, d, Extended Data Fig. 2d–g and Supplementary Tables 1, 4). We noted that while input sequence reads have a typical distribution along transcripts, m^1A immunoprecipitation reads pile up towards their 5′ ends (Extended Data Fig. 3a). To investigate this further, metagene profiles were generated in which gene segments were rescaled proportionally so that all segments of one kind appear to have the same length. This revealed that m^1A clusters sharply around the start codon to produce a remarkably similar profile in the three human cell lines (Fig. 2f). Over 50% of the peaks reside within a stretch of 300 nucleotides centred on the start codon (Extended Data Fig. 3b–g).

Ribosome profiling[19], and a recently modified version that captures initiating 80S ribosomes[20,21], have uncovered a surprising variety of alternative translation initiation sites (TISs). We examined our data sets from this perspective and found that methylated transcripts have, on average, more alternative TISs than non-methylated ones (1.98 versus 1.59 in HeLa; 2.37 versus 1.69 in HEK293), and that the number of m^1A sites per transcript positively correlates with the number of alternative TISs per transcript (Extended Data Fig. 4a–c). Furthermore, transcripts with upstream TISs are more likely to be methylated within the 5′ UTR, whereas transcripts with downstream TISs tend to be methylated within the CDS (Extended Data Fig. 4d, e). The distances of alternative TISs and respective m^1A peaks from the annotated start codon are well correlated, particularly those of upstream TISs and

5′ UTR m^1A peaks, suggesting that m^1A is associated with alternative TISs as well (Extended Data Fig. 4f–h). In summary, m^1A in human mRNA seems to be associated with a subset of TISs, both canonical and alternative, in all three cell lines examined.

To gain a deeper understanding of the underlying transcript attribute or processing event that potentially guides m^1A deposition to create the observed distribution, we binned methylated transcripts based on the exon that harbours the start codon and plotted the distribution of m^1A relative to the start codon. We observed an intriguing dissociation: when the start codon is in the 2nd or 3rd exons, m^1A tends to occur closer to the transcription start site (TSS) compared to when the start codon is in the 1st exon (Extended Data Fig. 3h). Whereas 5′ UTRs of transcripts with a start codon in downstream exons are on average longer (323 versus 189 nucleotides), their first splicing event tends to occur closer to the TSS (204 versus 359 nucleotides), mirroring m^1A behaviour. Therefore, we plotted the distribution of m^1A relative to the TSS in bins based on the length of the 1st exon and observed that m^1A moves away from the TSS as the length of the first exon increases (Extended Data Fig. 3i). These observations suggest that neither the TSS nor the start codon 'anchors' m^1A, but rather the first splice site does. We substantiated this by plotting m^1A relative to the nearest splice site (which is also the first splice site for 85% of m^1A peaks) and observed convergence of m^1A distribution in all start codon bins mostly upstream of the splice site, engendering the hypothesis that the first splicing reaction somehow guides m^1A deposition (Fig. 2g, Extended Data Fig. 3j). Analysis based on the smaller high- resolution m^1A trough data set recapitulated all the salient features of the methylome (Extended Data Fig. 3k–q, Supplementary Note 3 and Supplementary Table 6).

Conserved features of methylated transcripts

We next sought to identify sequence patterns that may define or associate with m^1A peak locations. GC content, a key determinant of RNA structure, is unusually high in m^1A peak areas that appear in all three transcript segments (Extended Data Fig. 5a). Several motif detection algorithms showed enrichment of GC-rich sequences with variable adenosine content, yet did not identify any specific motif *per se* (other than the 'AUG' itself which is expected to appear in peaks centred on the start codon) (Extended Data Fig. 5b). This suggests that a combination of sequence and structure features may specify methylation positions, perhaps similar to the case of m^1A deposition in tRNA[22,23]. We were able to identify and score single-nucleotide m^1A positions based on the change in mismatch rates between (1) untreated and alkaline-treated (m^1A-to-m^6A rearranged) immunoprecipitation sequence reads and between (2) input and immunoprecipitation (Supplementary Table 5). A sequence frequency logo of identified positions (Fig. 3a) and representative individual sequences (Extended Data Fig. 5c) demonstrate that m^1A sites are embedded in GC-rich environments. Using the m^1A trough data set we also identified a GA-rich motif that was present in 10–15% of the cases (Extended Data Fig. 3r).

Attributes of the 5′ UTR such as length, GC content, and associated minimum free energy (MFE), are known to affect the efficiency of translation initiation[24]. 5′ UTRs of methylated transcripts differ significantly from those of non-methylated ones in that their GC content is higher (median of 71% compared to 63.9%) (Extended Data Fig. 5d) and their length-

adjusted MFE (aMFE) is lower (median of −43.5 kcal mol^{-1} compared to −38.4 kcal mol^{-1}) (Fig. 3b, Extended Data Fig. 5e). We employed a sliding window approach to further characterize the continuous structural landscape of the AUG window (±150 nucleotides) in terms of GC content, MFE and experimental parallel analysis of RNA structure (PARS) score (Fig. 3c–e, Extended Data Fig. 5f, g). Both the experimental and calculated parameters agree that m^1A decorates highly structured AUG windows.

Evolutionary conservation and dynamics

Evolutionary conservation typically indicates a common fundamental biological function. We show above that m^1A is present in murine mRNA at comparable levels to those in human (Fig. 1b). Therefore, m^1A-seq was applied to RNA of mouse liver, mouse embryonic fibroblasts (MEFs) and mouse embryonic stem cells (mESC) (Supplementary Tables 2, 4). A previously unreported single m^1A position in mouse 28S rRNA was identified in an orthologous location to the known m^1A position in human 28S rRNA (Extended Data Fig. 6a–c). The mouse m^1A methylome closely resembles that of human: approximately 15% of adequately expressed genes are methylated, the majority of which carry a single m^1A (Fig. 4a), and the percentage of methylated genes increases with expression level (Fig. 4b). m^1A in mouse mRNA is non-randomly distributed along transcripts with dense clustering around translation initiation sites, mirroring the profile in human (Fig. 4c–d, Extended Data Fig. 6d–l), including the association with the nearest splice site (Fig. 4e, Extended Data Fig. 6m). Similarly, m^1A sites reside within a GC-rich context (Extended Data Fig. 7a, b), and the 5′ UTRs of methylated transcripts have a higher GC content and a lower aMFE than those of all other (unmethylated) transcripts (Fig. 4f and Extended Data Fig. 7c–f).

We systematically assessed the extent of m^1A peak conservation between human and mouse and found that it extends to the gene level: out of 1,338 identified mouse liver m^1A peaks that could be mapped to adequately expressed, orthologous positions in human HepG2 cells, 441 had an m^1A peak at the orthologous position, representing 33% overall conservation ($P < 1.3\times10^{-310}$, Mann–Whitney U test) (Fig. 4g, Extended Data Fig. 7g). The 5′ UTR and a 300-nucleotide window centred on the AUG codon exhibit the highest degree of conservation with 44–46% conserved peaks, compared to 3–16% in other gene segments (Fig. 4g).

We applied m^1A-seq to RNA of *Saccharomyces cerevisiae* and *Schizosaccharomyces pombe* to further examine this mark in simple eukaryotes, and found it to be present in their mRNA transcriptomes, albeit without the characteristic mammalian pattern (Extended Data Fig. 8a–g, Supplementary Tables 3, 4). Importantly, upon transfer to a nitrogen-source deficient medium the *S. pombe* methylome exhibited noticeable changes in the identity of methylated transcripts (some transcripts gained m^1A while others lost it), providing an example of how physiological conditions dynamically shape m^1A (Extended Data Fig. 8h, i). These results further demonstrate the conservation of m^1A as a mark in eukaryotic mRNA, although the distribution pattern and functions in lower eukaryotes could be different from mammals, as also observed for m^6A[25,26].

Next, using quantitative LC-MS/MS we surveyed a range of physiological perturbations that could alter the total m^1A level in mRNA of mammalian cells. We found that glucose or amino acid starvation reduced m^1A level by approximately threefold and twofold, respectively, as early as 4 h; that heat shock increased m^1A level by approximately 1.5-fold at 4 h; and that serum starvation resulted in only a modest change within the same time frame (Fig. 5a, Extended Data Fig. 9a, b). Of note, m^6A levels measured in parallel do not change, or change slightly in the opposite direction, suggesting that the response is m^1A-specific (Fig. 5a). m^1A-seq performed after 4 h of glucose starvation or heat shock uncovered a more complex picture: while the overall number of m^1A peaks decreased (by 17%) and increased (by 23%), respectively, mirroring the LC-MS/MS measurement, still some individual positions behaved in the opposite direction (Fig. 5b, c; Extended Data Fig. 9c, d).

The m^1A levels across various tissues obtained from a single mouse also showed significant variability, with kidney and brain possessing the highest m^1A level (about threefold higher than that measured in liver, for example) (Fig. 5d). A comparison between tissues from lean (wt/wt) and obese mice (ob/ob) revealed that brains of the former contain 75% more m^1A (Fig. 5d). In sum, m^1A in mRNA is a dynamic modification in response to certain stress conditions and potentially physiological signalling, and its level varies between different tissues.

SAM-dependent methyltransferases that install m^1A on tRNA and rRNA are known in eukaryotes[23,27]. These or related homologues could mediate mRNA m^1A methylation. FTO, the first RNA demethylase to be discovered, belongs to the AlkB family of proteins, and catalyses oxidative demethylation of m^6A in mRNA[28]. Other members of the AlkB family are known to perform oxidative demethylation of m^1A and m^3C lesions in DNA/RNA. In particular, ALKBH3 was shown to have a strong preference for single stranded DNA/RNA, and to demethylate m^1A in tRNA and mRNA *in vitro*[29,30]. In line with previous biochemical observations, overexpression of wild-type ALKBH3, but not of an inactive mutant, reduced m^1A levels in mRNA (Extended Data Fig. 9e). These results suggest that ALKBH3 and its homologues are likely candidates that could reverse m^1A in mRNA and contribute to its dynamic regulation.

m¹A correlates with elevated translation

Structure and sequence features of the 5′ UTR and both sides of the start codon affect the scanning process and thereby the efficiency of translation initiation and early elongation[31,32]. We show here that m^1A is a widespread and conserved post-transcriptional modification that is associated with TISs in thousands of mammalian transcripts characterized by structured 5′ UTRs. The precise localization of m^1A in an area of obvious regulatory importance, coupled with its ability to restructure RNA in other cases (such as tRNA[33]) and to affect RNA–protein interactions, points to possible involvement in translation initiation.

We used published ribosome profiling and proteomic data sets, obtained from the same cell lines and tissues used for m^1A profiling, to assess possible effects of m^1A on translation (see

Methods). The translation efficiency[19] (TE) and ribosome release score[34] (RRS) of genes with a single m^1A peak in the start codon window compared to genes devoid of m^1A altogether are significantly higher (~1.2–1.4, on average) in both human and mouse cells (Extended Data Fig. 10). Furthermore, correlation of m^1A with protein levels normalized to mRNA abundance reveals a similar trend: in all cell types examined, methylated genes tend to have higher protein levels than non-methylated genes (Fig. 6a–f). The average fold-change in protein levels between methylated and non-methylated genes in all cell types—and across all gene expression bins—is ~1.7. Considering that the average fraction of methylated transcripts is ~20%, the isolated true effect of m^1A could be even higher. The contribution of m^1A remains significant even after accounting for multiple covariates that are known to affect translation (ANCOVA, Supplementary Table 8).

Discussion

N^1-methylation on RNA adenosine occurs at the Watson–Crick interface and is expected to affect RNA base pairing[35]. In addition to an added methyl group, this modification also endows the modified adenosine with a positive charge under physiological conditions (Fig. 1a), which could markedly alter RNA structure and protein–RNA interactions. The impact of m^1A on the structure and function of tRNA is well documented, where a single m^1A can be essential for correct functional folding of a tRNA molecule[33]. A single charge difference has been shown to induce ~100–1,000-fold affinity difference of protein–DNA interactions[36]. We show here that m^1A is a modification occurring on thousands of mRNA transcripts in several human and mouse cell types, as well as on hundreds of transcripts in two yeast species. Applying m^1A-seq, a method relying on immunoprecipitation of m^1A-containing RNA fragments, we found a striking enrichment of m^1A around the start codon in human and mouse mRNA. Taking advantage of the Dimroth rearrangement, which converts m^1A (mutation prone in reverse transcription) to m^6A (low mutation rate in reverse transcription[37]) with alkaline treatment, we confirmed the accumulation of m^1A around the start codon at high resolution.

Transcriptome-wide mapping of m^1A revealed unique features of its distribution that strongly indicate functional roles: (1) m^1A resides close to both canonical and alternative TISs found mostly upstream of the first splice site; (2) m^1A is present in highly structured regions around the start codon; (3) m^1A positively correlates with translation efficiency and protein level; (4) the distribution pattern and m^1A peaks are highly conserved in all mouse and human cell types examined; and (5) m^1A is dynamic in response to certain stress, and potentially physiological, signals, and its level varies across mouse tissues. Together, these attributes suggest a positive and dynamic role for m^1A in translation initiation in mammalian cells. The importance of RNA structure in translation initiation is well appreciated[38]. A positively charged m^1A may alter the secondary/tertiary structure of mRNA around TISs by blocking Watson–Crick base pairing or introducing charge–charge interactions. Alternatively, potential binding proteins may specifically recognize m^1A and facilitate translation initiation of methylated transcripts in a way analogous to the role of the m^6A reader YTHDF1 in translation enhancement[39]. Either way, it is tempting to speculate that m^1A can modulate the strength of a particular translation initiation site, thereby affecting the balance between alternative and canonical initiation sites.

In contrast to m^6A, which is enriched around the stop codon and in the 3′ UTR[1,2], m^1A preferentially associates with the start codon region in mammalian mRNA. These two marks could complement each other in controlling mRNA metabolism and translation. A single m^6A modification usually induces ~10-fold change in either duplex stability or protein–RNA affinity, as would be expected by the presence of an extra methyl group[40,41]. The propensity of m^6A to cluster at 3′ UTRs also enables a wider range of dynamic tuning than a single m^6A site could offer[1,2]. The unique chemical properties of m^1A, with both a positive charge and a methyl group, potentially allow each individual modified site to have a stronger effect than m^6A in terms of RNA structure or protein–RNA interaction.

The discovery of this new mRNA mark that positively correlates with translation adds an exciting new dimension to post-transcriptional gene expression regulation mediated through mRNA modifications. While our paper was in proof, we were alerted to a study by Chengqi Yi and colleagues reporting similar findings on the m^1A methylome in a human cell line[42].

METHODS

Cells and tissues

Human HeLa (cervical adenocarcinoma), HepG2 (hepatocellular carcinoma) and HEK293 (embryonic kidney) cell lines (ATCC) and primary mouse embryonic fibroblasts (MEFs) (C57BL/6, ATCC) were maintained in DMEM (Thermo Fisher Scientific) containing 25 mM glucose, 4 mM -glutamine, supplemented with 100 U ml^{-1} penicillin, 100 μg ml^{-1} streptomycin and 10% FBS. Mouse embryonic stem cells (mESCs) were maintained in FBS-free N2B27-based media, as previously described[43]. Cells were routinely checked for mycoplasma contamination. Mouse tissues were obtained from wild-type and ob/ob C57BL/6 mice. For metabolic labelling, methionine-devoid DMEM was supplemented with L-methionine-(methyl-d_3) (Sigma-Aldrich).

Cell treatments

HepG2 cells were maintained as described above and subjected to the following growth conditions: (1) heat shock (43 °C for 4 h); (2) glucose starvation (glucose-depleted medium for 4 h); (3) amino acid starvation (amino acid-depleted medium, with or without 200 μM *S*-adenosyl-methionine (SAM) supplementation, for 4 h); and (4) serum starvation (serum-depleted medium for 4 h), following which they were immediately harvested in Cell Lysis Solution (5 Prime).

Yeast strains and growth conditions

Wild-type (BY4741) *S. cerevisiae* cells were grown vegetatively in YPD medium to mid-log phase and harvested. Wild-type heterothallic (Sp1) *S. pombe* cells were grown vegetatively in YES medium to mid-log phase and harvested. For induction of sporulation/arrest, Sp1 cells were washed and transferred to Edinburgh Minimal Medium lacking NH_4Cl (EMM-N) for 4 h and harvested.

RNA purification

Total RNA from cells in culture and mouse tissues was purified using PerfectPure RNA Cultured Cell Kit (5 Prime) and PerfectPure RNA Tissue Kit (5 Prime), respectively, and DNase-treated. Enrichment of polyadenylated RNA (polyA $^+$ RNA) from total RNA was carried out using one round of GenElute mRNA Miniprep Kit (Sigma-Aldrich). Ribo-Zero Gold rRNA Removal Kit (Illumina) was used to deplete rRNA from polyA$^+$ RNA before LC-MS/MS.

Dot blot assays

RNA Oligonucleotides were synthesized in-house with either m^1A, m^6A or A at a single internal position (5′-AC(m^1A/m^6A/A)UG-3′), spotted onto a nylon membrane (GE Healthcare) in decreasing amounts (1,000, 200, 40 and 8 pmol) and UV-crosslinked. Membranes were blocked with 5% non-fat dry milk in 1 × PBST (blocking buffer) for 1 h at 25 °C, and incubated overnight with either mouse anti-m^1A antibody (1 μg ml^{-1}, MBL) or rabbit anti-m^6A antibody (1 μg ml^{-1}, Synaptic Systems) in 1 × PBST at 4 °C. Following extensive washing with 1 × PBST, membranes were incubated with either HRP-conjugated goat anti-mouse IgG or anti-rabbit IgG antibody (1:2,500, Thermo Fisher Scientific) in blocking buffer for 1 h at 25 °C. Membranes were washed in 1 ×PBST, developed with ECL substrate (Thermo Fisher Scientific) and imaged with FluorChem imager (Protein Simple) or X-ray film. Competitive dot blots were performed on separate membranes spotted with 75 pmol of the m^1A-containing oligonucleotide by co-incubation of anti-m^1A antibody with increasing concentrations of either m^1A or m^6A competitor mononucleoside (0, 1, 2 and 4 μM).

m^1A detection and quantitation

Purified RNA (see ‘RNA purification’ section above) was subjected to liquid chromatography-tandem mass spectrometry (LC-MS/MS) for detection and accurate quantitation of m^1A, essentially as previously described[44]. 200–400 ng of purified RNA was digested by P1 nuclease (Wako, 2 U) in 40 μl of buffer containing 25 mM NaCl and 2.5 mM $ZnCl_2$ for 2 h at 37 °C. Subsequently, 5 units (1 μl) of Antarctic Phosphatase (New England Biolabs) and 1 × Antarctic Phosphatase reaction buffer were added and the sample was incubated for another 2 h at 37 °C. The sample was then filtered (0.22 μm, Millipore) and injected into a C18 reverse phase column coupled on-line to Agilent 6410 QQQ triple-quadrupole LC mass spectrometer in positive electrospray ionization mode. Quantitation was performed based on nucleoside-to-base ion transitions (268-to-136 for A; 282-to-150 for m^6A and m^1A (retention times of 2.5 and 0.9 min, respectively); 285-to-153 for d_3-m1A and d_3-m6A; 245-to-179 for Ψ; 245-to-113 for U) using standard curves of pure nucleosides and stable isotope-labelled internal standards (d_3-m1A and d_3-m6A), as previously described45–47.

Synthesis of stable isotope-labelled internal standards

d_3-m1A was synthesized following a previously described procedure for the synthesis of m^1A[48], replacing CH_3I with CD_3I. d_3-m6A was synthesized following a previously described procedure for the synthesis of m^6A[49,50], replacing CH_3NH_2 with CD_3NH_2.

m^{1}A-seq

Mapping of m^{1}A in total or mRNA was performed using m^{1}A-seq, which is based on the previously described m^{6}A-seq protocol[51] with the following modifications: RNA fragmentation was performed using RNA Fragmentation Reagents (Thermo Fisher Scientific) for 15 min at 70 °C to minimize m^{1}A-to-m^{6}A rearrangement followed by column purification (RNA Clean & Concentrator, Zymo). Anti-m^{1}A antibody (MBL) was pre-coupled to Protein G Dynabeads (Thermo Fisher Scientific) and used to immunoprecipitate methylated RNA fragments for 3 h at 4 °C. Fragment elution was carried out by either digestion with Proteinase K (Sigma-Aldrich; 5 units in 5 mM Tris pH 7.5, 1 mM EDTA and 0.25% SDS for 1.5 h at 37 °C) followed by TRIzol (Thermo Fisher Scientific) extraction of the supernatant and ethanol precipitation, or by competitive elution using m^{1}A mono-nucleoside (Santa Cruz Biotechnology), as in m^{6}A-seq. Induced m^{1}A-to-m^{6}A rearrangement was achieved by incubating the input and immunoprecipitation fragments in an alkaline buffer (50 mM Na_2CO_3, 2 mM EDTA, pH 10.4) for 1 h at 50 °C or 60 °C followed by column purification (RNA Clean & Concentrator, Zymo) (Extended Data Fig. 1m). Immunoprecipitated RNA fragments and comparable amounts of input were subjected to first-strand cDNA synthesis using the NEBNext Ultra RNA Library Prep Kit for Illumina (New England Biolabs). Sequencing was carried out on Illumina HiSeq2500 according to the manufacturer's instructions, using 10 pM template per sample for cluster generation, TruSeq SR Cluster kit v3 (Illumina), TruSeq SBS Kit v3-HS (Illumina) and TruSeq Multiplex Sequencing primer kit (Illumina). Summary of read numbers for each replicate can be found in Supplementary Table 4.

Validation of m^{1}A-seq

Reads were aligned to the 28S ribosomal RNA sequences of human (RefSeq NR_003287.2), mouse (RefSeq NR_003279/NCBI X00525) and *S. cerevisiae* (SGD RDN25-2, ID: S000006485.) using Bowtie2[52] with local alignment option (--local). Enrichment was calculated as the coverage ratio of immunoprecipitation to input. Mismatch rate was assessed using mpileup tool of the SAMtools software package (version 0.1.18)[53] for calling variants over the entire 28S transcript. The frequency of non-adenosine bases at each adenosine position and the coverage of each base in the transcript were reported.

RNA expression level

Reads per kilobase of transcript per million mapped reads (RPKM) expression levels of RefSeq genes were calculated using HTseq-count[54] and R package edgeR[55]. Fragments per kilobase of transcript per million mapped reads (FPKM) values were calculated by the CUFFLINKS tool (version 2.2.1)[56]. Only genes whose expression level was above the first quartile were considered adequately expressed and used for downstream analyses. Adequately expressed genes (RPKM) were divided into 10 expression bins for correlation with methylation and the fraction of methylated genes in each bin was calculated.

Peak calling

Adaptors and low quality bases were trimmed from raw sequencing reads using cutadapt[57]. Reads were aligned to the relevant genome (human-hg19, mouse-mm10, *S. pombe*-

ASM294v2.29, and *S. cerevisiae*-S288C with UTR data downloaded from http://genie.weizmann.ac.il/pubs/PARS10/pars10_catalogs.html) using Tophat2 (version 2.0.12)[58]. Peaks enriched in immunoprecipitation over input experiments were identified using MACS2 (version 2.1.0.20140616)[18]. MACS2-identified peaks were intersected with a database of exons of the relevant genome (RefSeq annotation). Peaks were allocated to the feature containing the segment with which they share the largest overlap. Peaks falling in intergenic sequences or having an overlap shorter than 50 nucleotides were excluded from further analyses. For each cell type only peaks identified (FC ≥2 or FC ≥4, as indicated, FDR ≤0.05) in replicates were considered. Common human peaks were defined as peaks independently identified in both HeLa and HepG2 RNA. Negative peaks were identified by switching the immunoprecipitation and input samples.

Coverage analysis

The coverage of unique reads at each nucleotide position at the transcriptomic level, in immunoprecipitation and input reads, was calculated and reported. Only transcripts in which at least one nucleotide exceeded a minimum depth of 10 reads in immunoprecipitation were used in further analysis for reduction of background noise. For whole-transcript coverage plots, each transcript was divided into 100 bins of equal length, and the median coverage for each bin across all transcripts was calculated.

m^1A stoichiometry

HepG2 mRNA was subjected to immunoprecipitation with anti-m^1A antibody in 2 biological replicates. Input and immunodepleted (unbound sup) RNA samples (75 ng each) were hybridized to PrimeView human gene expression microarrays (Affymetrix) and expression levels were determined. Genes expressed below the first quartile (as determined by mRNA-seq, see above) were set as the minimal intensity limit (blank), and only genes with intensities above this threshold were considered. To correct for technical loss of RNA during the different steps of the procedure, the average ratio of sup/input intensity was calculated for never-methylated genes (considering only genes that were unmethylated in all m^1A-seq experiments) and used for ratio correction of methylated genes carrying one m^1A peak. Fractional methylation level per gene was calculated as 1 – (corrected sup/input ratio).

Identification of m^1A-induced mismatches in m^1A peaks

Identification of sequence variants in m^1A peaks due to misincorporation at the m^1A position during reverse transcription was carried out by determining the base composition at each position within peak regions using bam-readcount (https://github.com/genome/bam-readcount). Identified adenosine positions (according to the encoding DNA strand) were then filtered to exclude known genomic polymorphism sites (dbSNP version 141) and identified A-to-I editing sites (Radar database). Variants were considered if the mismatch rate was greater than 0.1 and the overall coverage was greater than 20 reads. For HepG2 samples the fold enrichment of mismatch rate in untreated over rearranged sequence reads was calculated.

Trough identification

To identify points of lower coverage inside peak areas, we converted the bam files of the immunoprecipitation libraries to BigWig files and subjected them to PeakSplitter[59] with options of –valley 0.65 and –cutoff 30. The trough was identified as the minimal point ±10 nucleotides, between the summits of identified sub-peaks. Only troughs reoccurring in 3 biological repeats were considered.

Bidirectional conversion of genomic and transcriptomic coordinates

Genomic coordinates of all 5′ UTRs, CDS and 3′ UTRs of RefSeq transcripts were downloaded from the University of California, Santa Cruz genome browser (UCSC) table browser in BED format (hg19 and mm10 for human and mouse, respectively). Transcripts with IDs corresponding to more than one genomic location were discarded, as were transcripts of non-coding genes. Custom, in-house, awk and perl scripts were then used to convert transcriptomic coordinates to genomic coordinates and vice versa.

Definition of peak middle point

MACS2-generated genomic m^1A peak coordinates were converted to transcriptomic coordinates. Neighbouring peaks (at a distance of up to 10 nucleotides) on the same transcript were merged using mergeBed from the BEDTools package[60]. This allowed the unification of peaks overlapping more than one exon that were divided by MACS2 due to the presence of introns in genomic coordinates. The middle of the resulting transcriptomic peak was defined as peak middle and referred to as m^1A peak position in further analyses.

Metagene profiling

The relative position of each peak's middle point was located in the corresponding transcript segment (5′ UTR, CDS or 3′ UTR). Each segment was assigned a value corresponding to its average length fraction out of the overall transcript length. The corresponding relative peak position was then deduced within each segment and plotted along a normalized metagene profile with respect to the TSS, AUG start codon and stop codon positions. The distribution of m^1A peaks with respect to the canonical AUG start codon, TSS, first and nearest splice sites, and stop codon was also drawn in actual nucleotide distances.

Sliding window analysis of AUG start codon window

Structural features of a 300-nucleotide window centred on the AUG start codon were compared between methylated and non-methylated RefSeq genes. GC content was calculated as the average percent in a sliding window of 3 nucleotides. Local free energy (ΔG) was calculated in a 30-nucleotide consecutive jumping window (in steps of 10 nucleotides) using the RNAfold tool in the ViennaRNA package[61] with default parameter settings.

Minimum free energy (MFE) calculation

The 5′ UTR sequence of the predominant isoform of each gene (the highest expressed isoform in the input sample) was used to calculate GC content, MFE, length-adjusted MFE

(aMFE) and MFE density (MFEden) using the ViennaRNA package[61] and as previously described[62].

PARS-seq and PARS scores calculations

Parallel analysis of RNA structure (PARS) was performed as previously described[63] on HepG2 polyA$^+$ RNA. Reads were mapped to the human transcriptome (UCSC known canonical genes) using Bowtie2[52] with local alignment option (--local). Only uniquely aligned reads were used for analysis. Read start positions were counted for each base in the transcrip-tome, as the read start is +1 to the nuclease cleavage site and therefore informative regarding local RNA 2D structure[64]. Only reads with more than 5 consecutive bases matching the transcript at the start of the read were counted. Read counts were normalized to the respective library size. PARS-scores were then calculated based on the following equation:

$$\text{PARS- score}(i,j)=\log_2(V1'_{ij}/S1'_{ij})$$

$V1'_{ij}$ and $S1'_{ij}$ are the normalized read-start counts at base (i) in transcript (j) for V1 or S1, respectively.

PARS scores at the region around the start-codon (±150 nucleotides from the AUG) were averaged and used for a metagene analysis.

Motif search

To search for a motif, 101-nucleotide sequences in the AUG start codon window, centred on m^{1}A peaks in HeLa and mouse liver, were used. Compatible background sequences were used to prevent skewing of the results due to over-representation of known motifs in the region of the start codon, such as Kozak sequences and the AUG. The findMotifs program from the HOMER package[65] was then run using the settings -rna -len 6,7,8,9,10 –noweight. The same peak areas were used with MEME[66] for *de novo* motif enrichment analysis, with the settings -dna -minw 6 -maxw 10 -evt 0.01 -maxsize 1,000,000. A similar analysis was performed on m^{1}A peaks falling in the CDS with background sequences randomly generated from non-methylated exons. 199 sequences of 20 nucleotides, surrounding the mutations identified above, were used to create a frequency plot of the nucleotides surrounding the mutation sites using WebLogo[67].

Comparison of m^{6}A and m^{1}A profiles

m^{1}A and m^{6}A peaks[1,42,68] were intersected using BEDTools[60]. Similarity between sets was also evaluated by comparing the metagene profiles of the two modifications.

TIS correlation

TISs data was downloaded from http://www.ncbi.nlm.nih.gov/sra?term=SRA160745 (ref. 21) and genomic locations were converted to transcriptomic locations (as described above). For each alternative TIS, the closest m^{1}A peak was identified and the distance of both from the canonical AUG start codon was calculated. Correlation of alternative TISs with the

number of m^1A peaks per gene was carried out by dividing the genes containing alterative TISs to bins according to the number of peaks per gene.

Gene ontology (GO) enrichment

Methylated gene RefSeq IDs were uploaded to DAVID Bioinformatics Resources (http://david.abcc.ncifcrf.gov) and functional enrichment analysis was performed using all adequately expressed genes as background. Resulting enriched GO terms were restricted to fold enrichment ≥1.5, Bonferroni corrected $P \leq 0.005$.

Human–mouse conservation

m^1A mouse liver peaks were converted to the homologous coordinates in the human hg19 genome, using the LiftOver tool of the UCSC genome browser[69]. To assess the significance of these results we chose at random an equal number of 200 bp sized areas from within mouse genes that have a human orthologue. The areas were chosen from all gene segments in the same proportion as observed in the original data set. Randomly chosen areas were similarly converted and intersected with HepG2 m^1A peaks. To calculate the statistical significance the randomization was repeated 1,000 times and Mann–Whitney *U* test was used.

ALKBH3 overexpression

Plasmids encoding wild-type and mutant (D193A) FLAG-tagged human ALKBH3 were transfected into 293 Freestyle cells using polyethylenimine (PEI; Polysciences, Inc.) at a ratio of 3 μl PEI per 1 μg plasmid DNA. After 24 h, cells were pelleted and washed once with cold PBS before being lysed in Cell Lysis Solution (5 Prime). mRNA was purified and digested for LC-MS/MS analysis as described in the 'RNA purification' and 'm^1A detection and quantitation' sections above.

Translation efficiency (TE) and ribosome release score (RRS)

Sequencing data was downloaded: for HEK293, mouse liver and MEFs - SRA160745[21], http://www.ncbi.nlm.nih.gov/sra?term=SRA160745; for mESCs - GSE30839[19], http://www.ncbi.nlm.nih.gov/geo/query/acc.cgi?acc=GSE30839. Reads were aligned and FPKM values were calculated (see above). For TE calculation, the Ribo-Seq FPKM of the most highly expressed transcript of each gene was divided by the mRNA-Seq FPKM of the same transcript. Only transcripts with FPKM and Ribo-Seq FPKM above first quartile were considered. TE data for mESCs was downloaded as-is from the original paper[19]. TE and RRS for HeLa were calculated using our published data[44]. RRS values were calculated using mRNA-Seq and Ribo-Seq reads as described previously[34,42].

Protein abundance

All protein abundance data analysed in this study was downloaded from the MOPED database (Multi-Omics Profiling Expression Data, https://www.proteinspire.org): HeLa, HepG2, HEK293 (Experiment ID: Geiger_MCP_2012)[70], and mouse liver (Experiment ID: Baylor_mouse_liver_profiling), or from Supplementary Data (mESCs[71] and MEFs[72], corrected as described[73]). For all cell types, excluding mESCs, we used the normalized

abundances as provided. For mESCs, raw intensities were divided by each leading protein molecular weight. Protein abundance data was then $\log_2$ transformed and subjected to an analysis of variance (ANOVA) with mRNA expression (FPKM) percentile bins for start m^1A and non-m^1A genes. For MEFs, the published mRNA expression data was used along with the corresponding protein abundance. Genes with mRNA expression below the lowest expressed gene containing m^1A or with FPKM < 0.2 were discarded.

Analysis of covariance (ANCOVA)

ANCOVA was calculated for genes methylated at the AUG start codon window (start m^1A) versus unmethylated genes (non-m^1A) as a fixed factor against $\log_2$ protein abundances, while cleaning the contribution of the following covariates: $\log_2$ mRNA expression, TIS Kozak score[74], MFE calculated by RNAfold and divided by 5′ UTR length, G-quadruplex motif in 5′ UTR[75,76], 5′ TOP motif in 5′ UTR from UTRdb (http://utrdb.ba.itb.cnr.it/), number of conserved miR sites (PCT score < 0) from TargetScan[77], and number of u/dTISs and u/dAUGs in human and mouse form QTI-seq[21]. The remaining factors, % GC Content in 5′ UTR, length of 5′ and 3′ UTRs, and number of exons in 5′ and 3′ UTRs were downloaded and calculated from the UCSC genome browser (hg19 and mm10). We considered the most expressed RefSeq genes in our data for unique transcript-associated parameters and gene symbols for general features. Variables were examined for linearity with protein output and for normal distribution. Log transformations were employed where appropriate. Tolerance was kept above 0.2 for all variables.

Extended Data

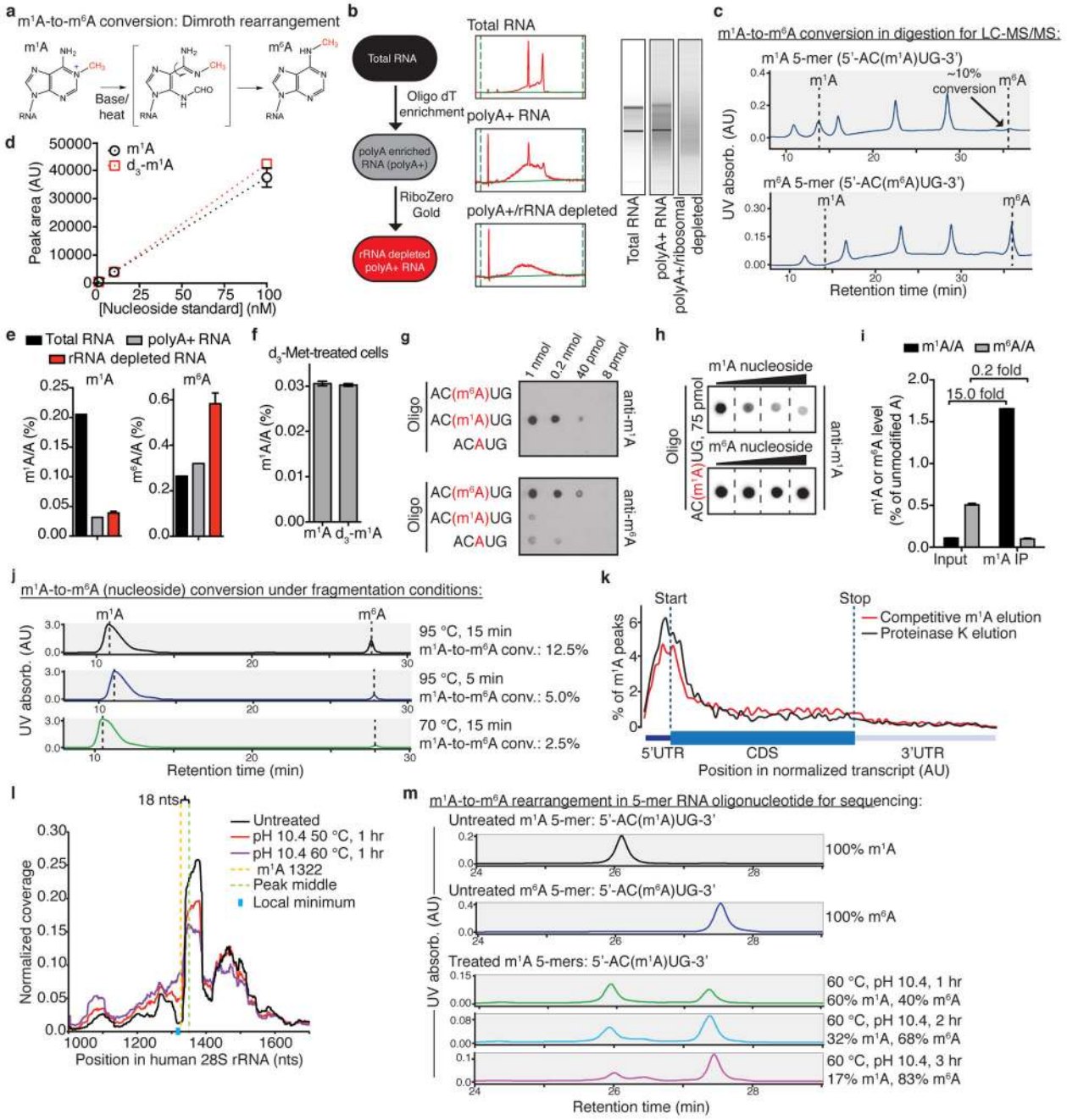

Extended Data Figure 1. Experimental conditions for detection, quantitation and sequencing of m^{1}A in mRNA

a, Schematic illustration of m^{1}A-to-m^{6}A rearrangement (Dimroth rearrangement) under alkaline conditions at elevated temperatures. **b**, mRNA purification scheme before LC-MS/MS m^{1}A quantitation (left). Corresponding RNA electrophoresis profiles obtained by Agilent 2100 Bioanalyzer (middle and right). **c**, Monitoring m^{1}A-to-m^{6}A rearrangement levels during sample preparation for LC-MS/MS. Synthetic 5-nucleotide long RNA

oligonucleotides containing m^1A (upper panel) or m^6A (lower panel) were digested to mononucleotides, dephosphorylated (see methods) and analysed by HPLC-UV. Only minimal (<10%) m^1A-to-m^6A rearrangement was observed (arrow). **d**, Standard curves for m^1A and deuterium-labelled m^1A (d_3-m1A) demonstrate very similar detection sensitivity in LC-MS/MS. Mean values ± s.e.m. are shown, $n = 3$. **e**, The change in m^1A/A and m^6A/A molar ratios (%) during the purification scheme outlined in **b**. Mean values ± s.e.m. are shown, $n = 3$. **f**, LC-MS/MS of mRNA isolated from HepG2 cells labelled with deuterated methionine (d_3-Met) for 24 h detects d_3-m1A, suggesting *S*-adenosyl-methionine (SAM) is the methyl donor. Mean values ± s.e.m. are shown, $n = 3$. **g**, Dot blots demonstrating high anti-m^1A antibody specificity. Increasing amounts (indicated above the top blot) of synthetic RNA oligonucleotides containing m^1A, m^6A or unmodified A residues were spotted onto a membrane and probed with either anti-m^1A or anti-m^6A antibodies. Anti-m^1A antibody detects m^1A and does not exhibit cross-reactivity with m^6A or A (upper blot); anti-m^6A antibody demonstrates low, yet detectable, cross-reactivity with both m^1A and A (lower blot). For blot source data, see Supplementary Fig. 1. **h**, Competitive dot blots were performed on separate membranes spotted with 75 pmol of synthetic m^1A-containing RNA oligonucleotide. Whereas increasing concentrations of free m^1A mononucleoside progressively attenuate anti-m^1A binding, increasing concentrations of free m^6A mononucleoside do not. For blot source data, see Supplementary Fig. 1. **i**, Quantitative LC-MS/MS demonstrates m^1A enrichment—and m^6A depletion—following immunoprecipitation (IP) with anti-m^1A antibody compared to total RNA input. Mean values ± s.e.m. are shown, $n = 3$. **j**, Monitoring m^1A-to-m^6A rearrangement levels under different RNA fragmentation conditions for use in m^1A-seq. Pure m^1A mononucleoside in 1×fragmentation buffer (see Methods) was subjected to the conditions specified to the right of the chromatograms and directly analysed by injection to HPLC-UV for rearrangement to m^6A. **k**, Comparison of competitive m^1A elution and Proteinase K elution of immunoprecipitated m^1A-containing RNA fragments from anti-m^1A-coupled magnetic beads shows that the two elution modes are equivalent. **l**, Identification of the known m^1A site in position 1322 of human 28S rRNA validates the accuracy of m^1A-seq and the use of peak middle points as a close approximation for m^1A sites. Partial m^1A-to-m^6A rearrangement increases the coverage around this site. **m**, Conditions for induced m^1A-to-m^6A rearrangement of RNA oligonucleotides that maintain RNA integrity for use in m^1A-seq. A synthetic 5-nucleotide long RNA oligonucleotide of the sequence 5′-AC(m^1A)UG-3′ was subjected to various base/heating conditions (indicated to the right of the chromatograms) and directly analysed by injection to HPLC-UV for rearrangement to 5′-AC(m^6A)UG-3′. Incubation at pH 10.4, 60 °C for 1 h results in rearrangement to m^6A in 40% of oligonucleotides; longer incubation times result in increased rates of rearrangement. Chromatograms of untreated RNA oligonucleotides appear above and mark the expected retention times.

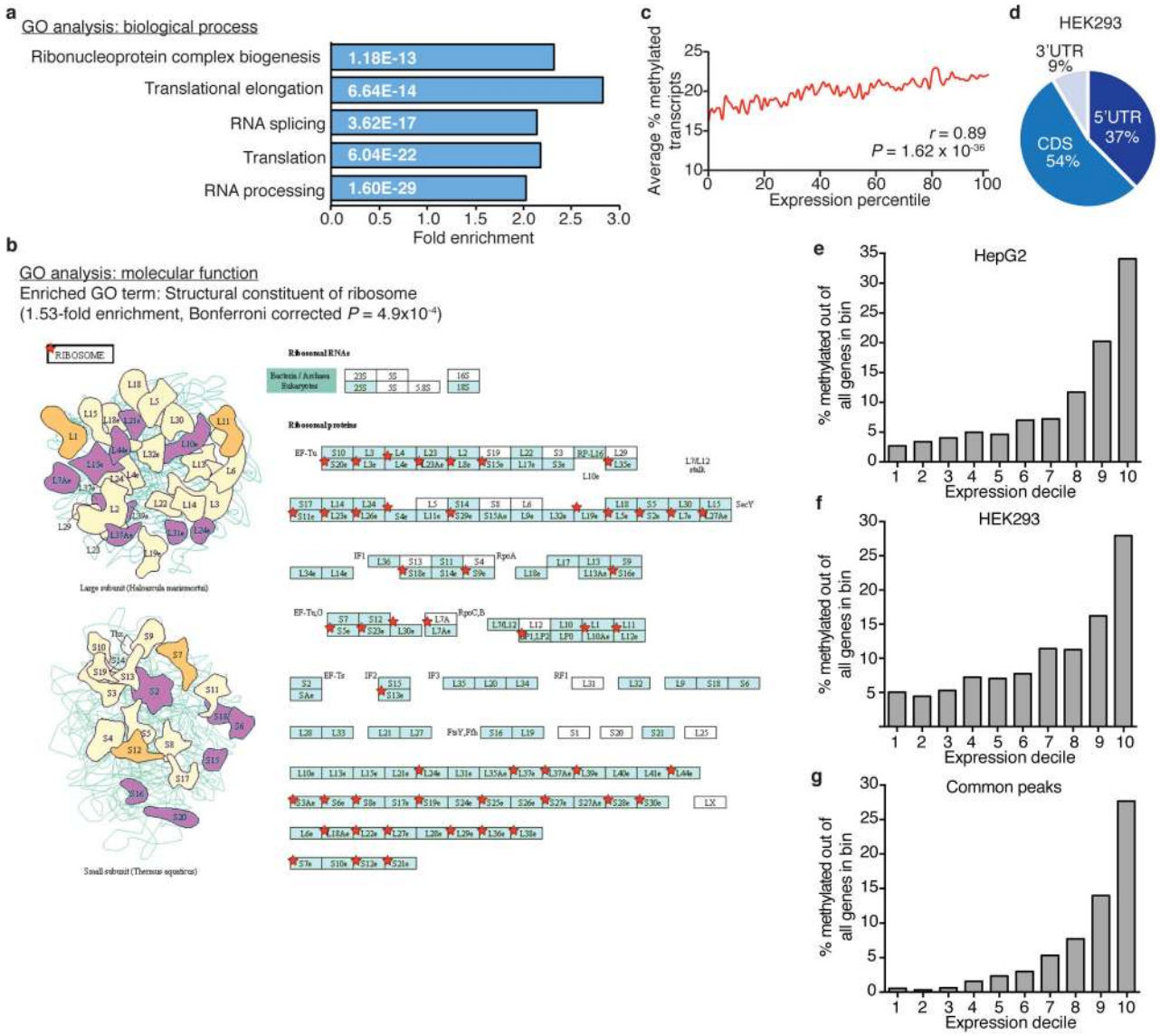

Extended Data Figure 2. Characterization of human m^{1}A-methylated genes

a, Gene ontology (GO) analysis of methylated HeLa genes relative to all adequately expressed genes (above the 1st quartile) reveals enrichment of biological processes related to translation and RNA metabolism. Fold-enrichment and *P* values are indicated for each category. **b**, GO analysis of molecular functions reveals enrichment of structural constituents of the ribosome. Scheme based on an illustration obtained from DAVID bioinformatics website of the KEGG human ribosome pathway. Red stars indicate methylated genes in the pathway. Colouring of the boxes and ribosome constituents is according to KEGG pathway maps showing interacting proteins and hyperlinks to gene entries that can be reached through http://www.genome.jp/kegg-bin/show_pathway?hsa03010. **c**, The average fraction of methylated transcripts (stoichiometry) increases with gene expression level. *r* and *P* values are indicated, Pearson correlation. **d**, Pie chart presenting the fraction of m^{1}A peaks in each of three non-overlapping transcript segments (5′ UTR, CDS and 3′ UTR) in HEK293

cells. **e**–**g**, The fraction of methylated genes increases with gene expression levels in HepG2 (**e**), HEK293 (**f**) and common human peaks (see Methods) (**g**).

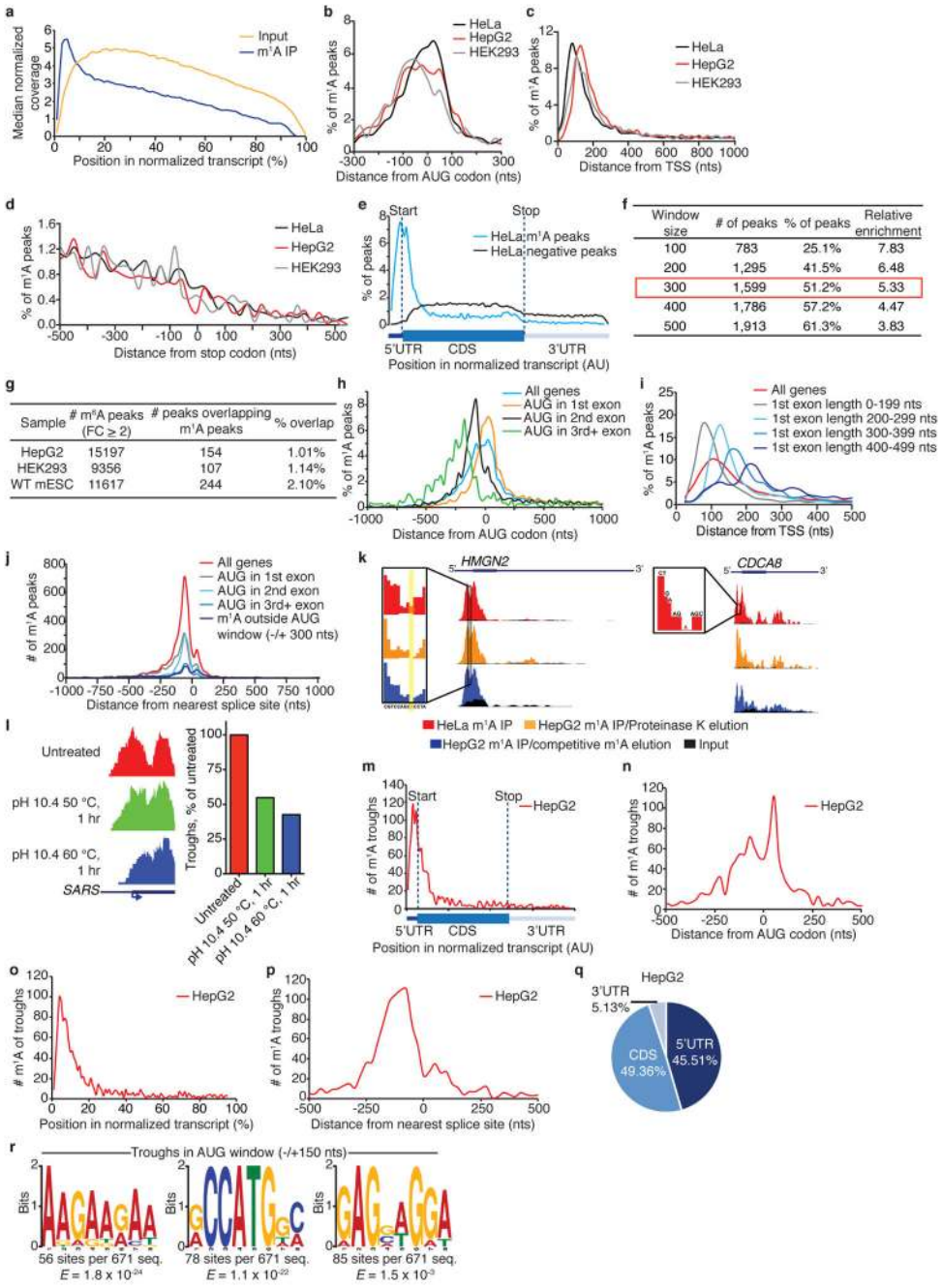

Extended Data Figure 3. Metagene analyses of human m^{1}A peaks

a, Metagene profiles demonstrating sequence coverage along a normalized gene transcript. Sequence reads of m^{1}A immunoprecipitation and input in HeLa cells are indicated in blue and orange, respectively. **b**–**d**, Metagene profiles of m^{1}A peak distribution in a non-normalized window centred on the AUG start codon (**b**), extending downstream from the

transcription start site (TSS) (**c**) and centred on the stop codon (**d**), in the indicated human cell types. **e**, Metagene profiles comparing the distribution of m^1A peaks (blue) to that of negative peaks (black) along a normalized transcript composed of three rescaled non-overlapping segments illustrated below, in HeLa cells. **f**, Table demonstrating m^1A peak enrichment in growing windows centred on the AUG start codon in HeLa cells. Enrichment is calculated as number of peaks in the window divided by window size (nucleotides). **g**, Table summarizing the overlap between m^6A and m^1A peaks in HepG2, HEK293 and WT mESCs. m^6A peaks are sourced from Dominissini *et al.*[1], Linder *et al.*[67] and Geula *et al.*[42], respectively. m^1A peaks are from the current study. **h**, **i**, Metagene profiles of m^1A peak distribution in a non-normalized window centred on the AUG codon (**h**) and extending downstream from the TSS (**i**). Peaks are sorted by the exon containing the AUG codon and the length of the first exon, respectively. **j**, Metagene profiles of m^1A peak distribution in a non-normalized window centered on the nearest splice site. Peaks are sorted by the exon containing the AUG codon in that gene. **k**, m^1A-induced reverse transcription (RT) arrests produce typical m^1A peaks characterized by a central region of reduced coverage with a local minimum (m^1A trough) Examples are shown. **l**, m^1A-to-m^6A rearrangement results in a reduced number of identified m^1A troughs. Higher rates of rearrangement further reduce the number of identified m^1A troughs (right panel). Example is shown (left panel). **m**, Metagene profile of m^1A trough distribution along a normalized transcript composed of three rescaled non-overlapping segments illustrated below, in HepG2 cells. **n**, Metagene profile of m^1A trough distribution in a non-normalized window centred on the AUG start codon in HepG2 cells. **o**, Metagene profile of m^1A trough distribution along a normalized transcript in HepG2 cells. **p**, Metagene profile of m^1A trough distribution in a non-normalized window centred on the nearest splice site in HepG2 cells. **q**, Pie chart presenting the fraction of m^1A troughs in each of three non-overlapping transcript segments (5′ UTR, CDS and 3′UTR) in HepG2 cells. **r**, MEME motifs identified in 100-nucleotide windows centred on m^1A troughs that lie within the AUG start codon window (±150 nucleotides) in HepG2 cells.

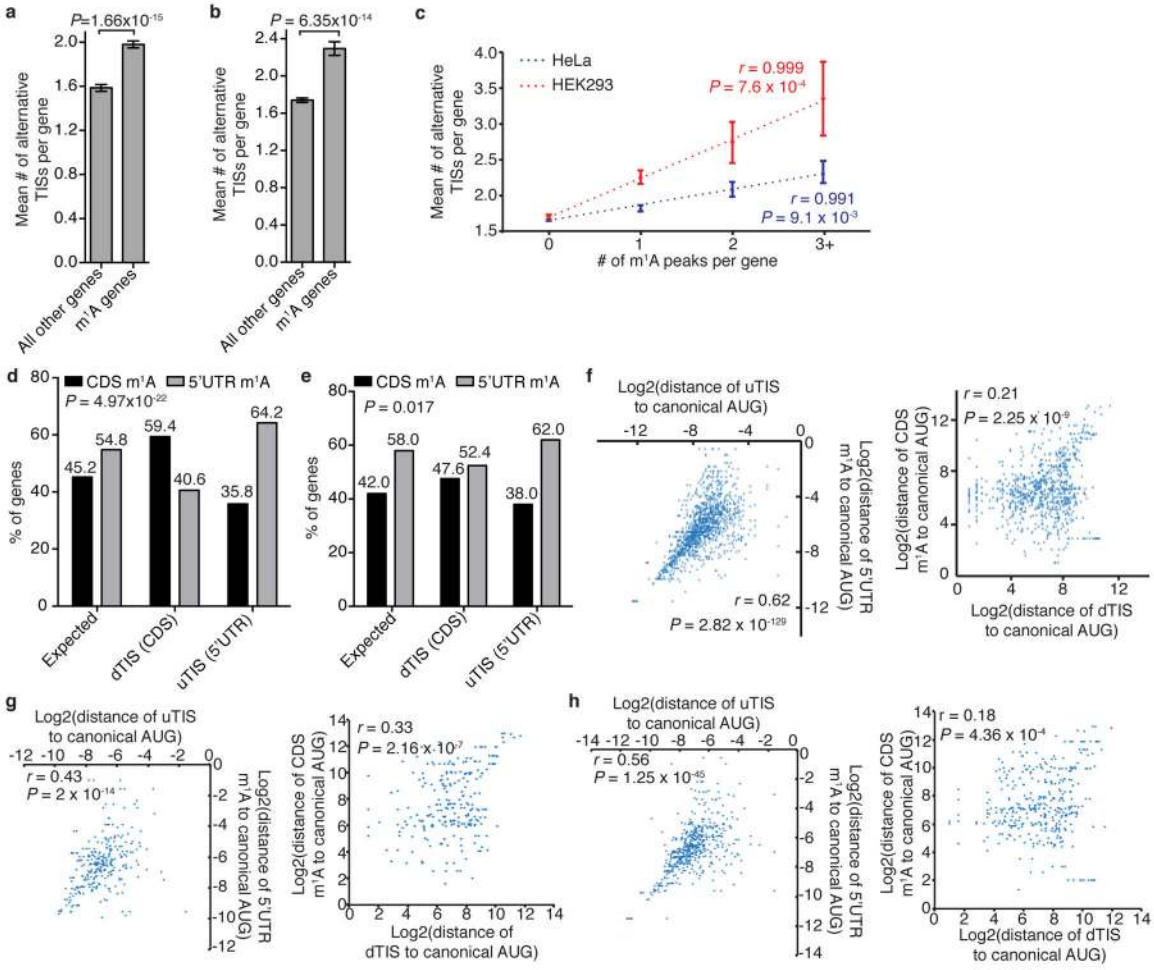

Extended Data Figure 4. Correlation between m^{1}A sites and TISs in human

a, **b**, The mean number of alternative TISs in methylated (m^{1}A) versus all other (unmethylated) genes in HeLa (**a**) and HEK293 (**b**) cells. Mean values ± s.e.m. are shown. *P* values are indicated, Mann–Whitney *U* test. **c**, The mean number of alternative TISs per gene as a function of the number of m^{1}A peaks per gene in HeLa and HEK293 cells. Mean values ± s.e.m. are shown; *r* and *P* values are indicated, Pearson correlation; regression line is drawn. **d**, **e**, The percentage of genes with upstream (=5′ UTR) or downstream (=CDS) m^{1}A sites out of all genes that have either downstream or upstream TISs, compared to the expected percentage in HeLa (**d**) and HEK293 (**e**) cells. *P* values are indicated, χ^2 test. **f**–**h**, Scatter plots showing the correlation between the locations ($\log_2$) of alternative TISs and m1A peaks with respect to the canonical AUG start codon (0) in HeLa (**f**), HEK293 (**g**) and HepG2 (**h**) cells: left, upstream TISs (uTIS) and 5′ UTRs m^{1}A peaks; right, downstream TISs (dTIS) and CDS m^{1}A peaks. *r* and *P* values are indicated, *t*-test.

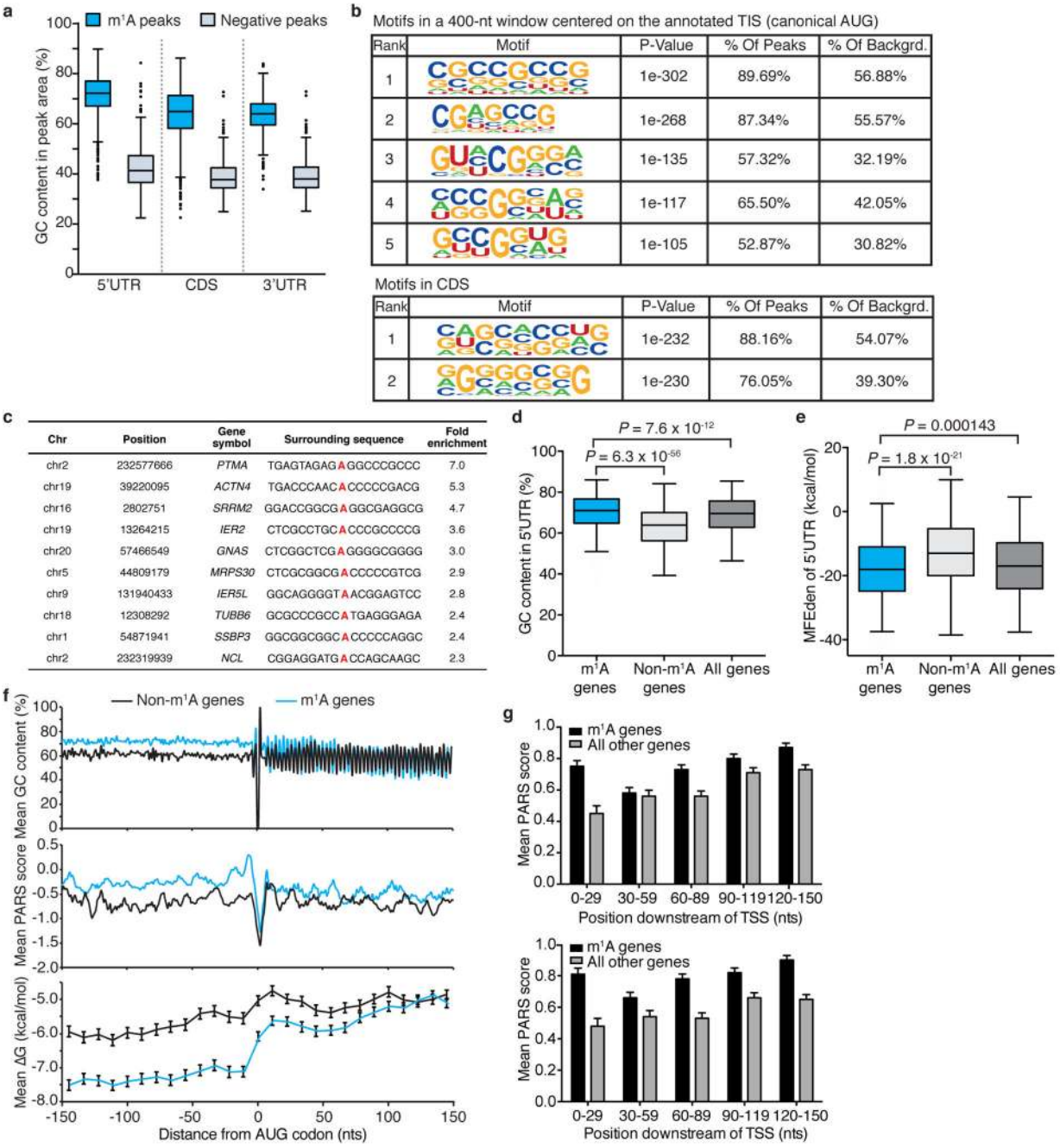

Extended Data Figure 5. Structure and sequence features of m^{1}A sites in human mRNA

a, m^{1}A peaks have a significantly higher GC content compared to negative peaks in all three transcript segments: 5′ UTR, CDS and 3′ UTR. Box limits represent 25th percentile, median and 75th percentile, whiskers represent 2.5 and 97.5 percentiles, and dots indicate outliers. $P = 1.5 \times 10^{-278}$, $P = 8.2 \times 10^{-259}$ and $P = 3.3 \times 10^{-271}$, respectively, *t*-test. **b**, Motifs identified in 400-nucleotide windows centred on the canonical AUG start codon in genes with m^{1}A peaks in this window (upper table), or around m^{1}A peaks located in the CDS, outside the AUG start codon window (lower table). **c**, Examples of adenosines around m^{1}A

peak middles with increased mismatch rates. Fold-enrichment values are the ratios of mismatch rates in untreated relative to rearranged samples. The top ten highest fold enrichment samples are shown. **d**, **e**, GC content (**d**) and minimum free energy density (MFEden) (**e**) of 5′ UTRs of methylated (m^1A), unmethylated (Non-m^1A) and all genes. Box limits represent 25th percentile, median and 75th percentile, whiskers represent 2.5 and 97.5 percentiles. *P* values are indicted, *t*-test. **f**, Mean GC content (upper panel), PARS score (middle panel) and free energy (ΔG, lower panel) in a 300-nucleotide window centred on the start codon of commonly methylated genes relative to non-methylated genes (see Methods). Error bars represent s.e.m. **g**, The PARS scores of methylated compared to all other genes in HepG2 cells in a 150-nucleotide window extending downstream from the TSS, calculated in 30-nucleotide sliding windows. Each plot represents data from an independent PARS experiment. Error bars represent s.d.

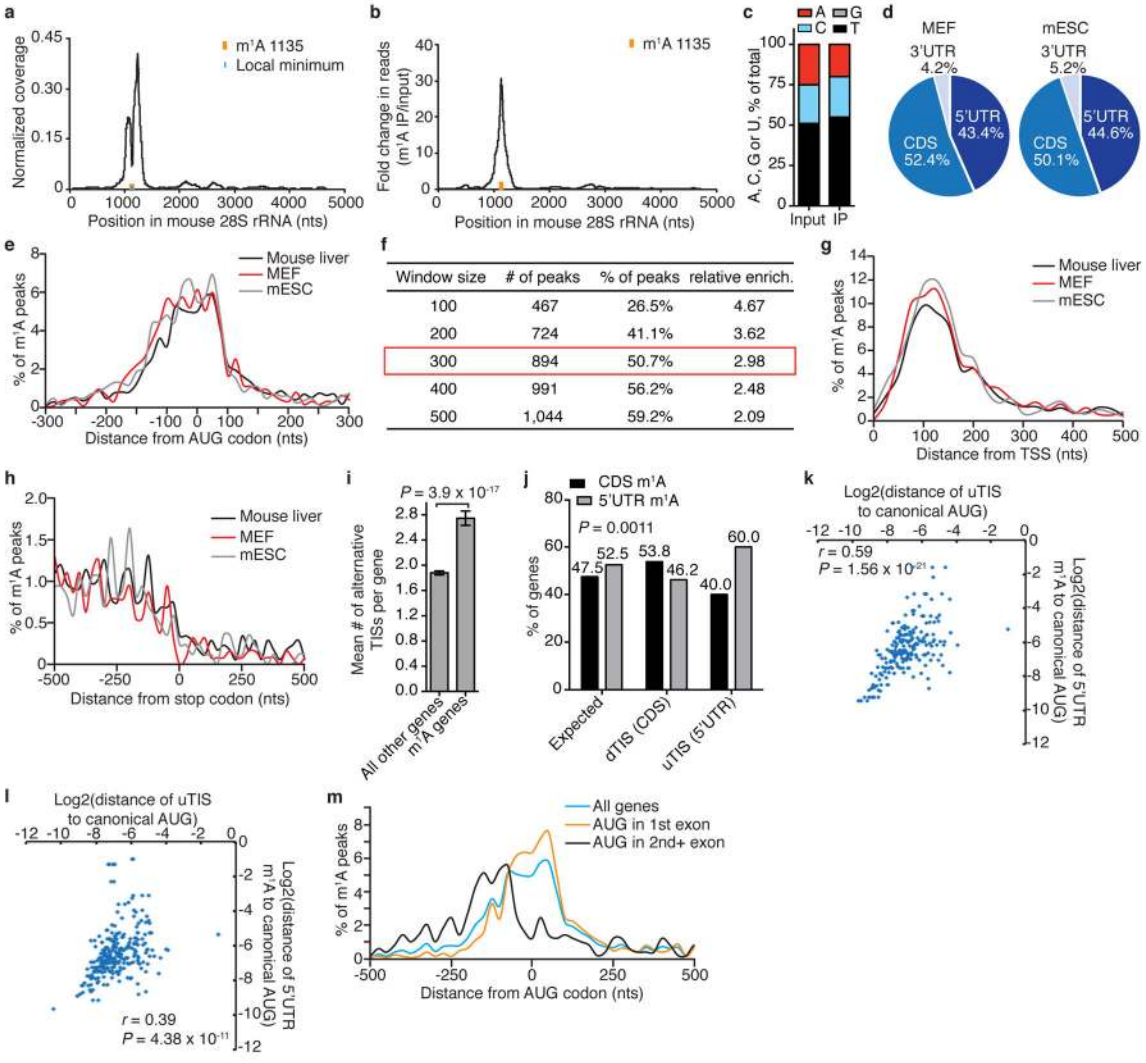

Extended Data Figure 6. Features of the mouse m^1A methylome (part 1)

a, Detection of an m^1A site at position 1135 of mouse 28S rRNA, in mouse liver m^1A immunoprecipitation. A drop in sequence read coverage can be seen at the methylated

position. **b**, Fold-enrichment (immunoprecipitation over input reads) identifies an m^1A peak. **c**, High mismatch rate at the identified m^1A 1135 in mouse 28S rRNA. **d**, Pie charts presenting the fraction of m^1A peaks in each of three non-overlapping transcript segments (5′ UTR, CDS and 3′ UTR) in the indicated mouse cell types. **e**, Metagene profiles of m^1A peak distribution in a non-normalized window centred on the AUG start codon in the indicated mouse cell types. **f**, Table showing m^1A peak enrichment in growing windows centred on the AUG start codon in mouse liver. Enrichment is calculated as the number of peaks in the window divided by window size (nucleotides). **g**, **h**, Metagene profiles of m^1A peak distribution in a non-normalized window extending downstream from the TSS (**g**) and centred on the stop codon (**h**) in the indicated mouse cell types. **i**, The mean number of alternative TISs in methylated (m^1A) versus all other (unmethylated) genes in MEF cells. Mean values ± s.e.m. are shown; *P* value is indicated, Mann–Whitney *U* test. **j**, The percentage of genes with upstream (=5′ UTR) and downstream (=CDS) m^1A sites out of all genes that have either downstream or upstream alternative TISs, compared to the expected percentage in MEF cells. *P* value is indicated, χ^2 test. **k**, **l**, Scatter plots showing the correlation between the locations ($\log_2$) of upstream TISs (uTIS) and 5′ UTR m^1A peaks relative to the canonical AUG start codon (0) in mouse liver (**k**) and MEF (**l**) cells. *r* and *P* values are indicated, *t*-test. **m**, Metagene profiles of mouse m^1A peak distribution in a non-normalized window centred on the AUG codon. Peaks are sorted by the exon containing the AUG codon in that gene.

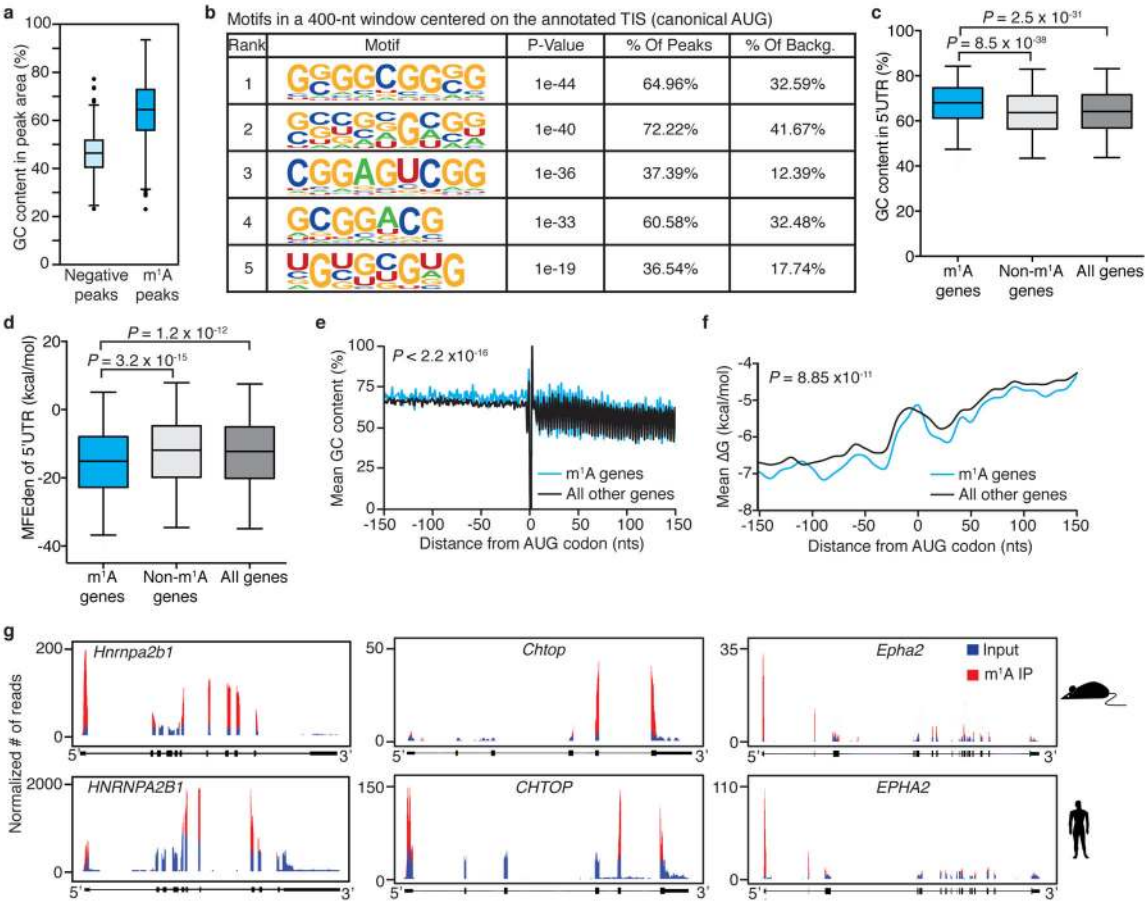

Extended Data Figure 7. Features of the mouse m^{1}A methylome (part 2)

a, Mouse m^{1}A peaks have a significantly higher GC content compared to negative peaks. Box limits represent 25th percentile, median and 75th percentile, whiskers represent 2.5 and 97.5 percentiles, and dots indicate outliers. P=4.4 ×10 $^{-175}$, t-test. **b**, Motifs identified in 400-nucleotide windows centred on the canonical AUG start codon in genes with m^{1}A peaks in this window in mouse liver. **c**, **d**, GC content (**c**) and MFEden (**d**) of 5′ UTRs of methylated (m^{1}A), unmethylated (Non-m^{1}A) and all genes. Box limits represent 25th percentile, median and 75th percentile, whiskers represent 2.5 and 97.5 percentiles. P values are indicted, t-test. **e**, **f**, A sliding window profile of mean GC content (**e**) and mean ΔG (**f**) in a 300-nucleotide window centred on the canonical AUG start codon in methylated (m^{1}A) genes compared to all other genes in mouse liver. P values are indicated, Kolmogorov–Smirnov test and t-test. **g**, Representative plots of human-mouse orthologous genes with conserved m^{1}A peaks. Plot format as in Fig. 2a.

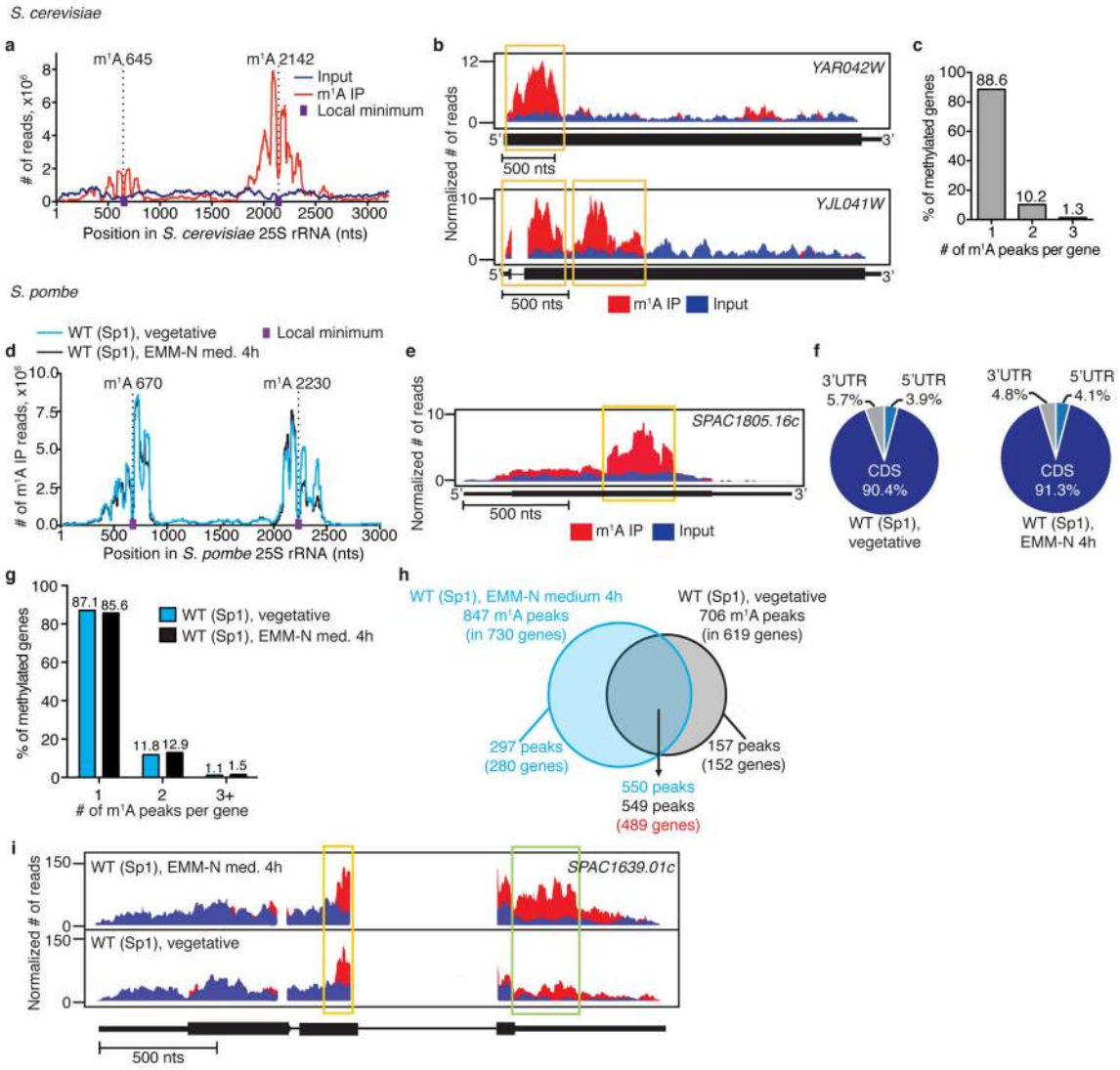

Extended Data Figure 8. The yeast m^{1}A methylome

a, m^{1}A-seq identifies the known m^{1}A sites (645 and 2142) in *S. cerevisiae* 25S rRNA. A drop in sequence read coverage (indicated by purple dots) occurs around the methylated positions (indicated by dashed lines). **b**, Representative plots of methylated transcripts in *S. cerevisiae*. Plot format as in Fig. 2a. **c**, The percentage of methylated genes that carry 1, 2 or 3 m^{1}A peaks per gene in *S. cerevisiae*. Out of 843 m^{1}A peaks (FC ≥4, FDR ≤5%) in 778 genes, most (88.6%) are methylated only once. Unlike in mammals, m^{1}A is distributed across the coding transcriptome without an apparent preferred location. **d**, m^{1}A-seq identified the known m^{1}A sites (670 and 2230) in *S. pombe* 25S rRNA. A drop in sequence read coverage (indicated by purple dots) occurs around the methylated positions (indicated by dashed lines). **e**, Representative plot of a methylated transcript in *S. pombe*. Plot format as in Fig. 2a. **f**, Pie charts presenting the fraction of m^{1}A peaks in each of three non-overlapping transcript segments (5′ UTR, CDS and 3′ UTR) in *S. pombe* Sp1 strain under the indicated conditions. Under vegetative growth, we identified 706 m^{1}A peaks (FC ≥4, FDR ≤5%) in 619 gene transcripts, most of which (90.4%) distributed along the CDS. Four

hours after transfer to a nitrogen-source deficient 'sporulation' medium, 157 out of the vegetative state m^{1}A peaks were no longer detected, and 297 new peaks appeared. Importantly, transcripts that harbour differential peaks were adequately expressed (above the 1st quartile) in both conditions. **g**, The percentage of methylated genes that carry 1, 2, or 3 +m ^{1} A peaks per gene in *S. pombe* Sp1 strain under the indicated conditions. **h**, Venn diagram representing differential and shared m^{1}A peaks in *S. pombe* Sp1 strain under the indicated conditions. **i**, Representative plots of a differentially methylated transcript in *S. pombe* Sp1 strain under the indicated conditions. Yellow box, conserved peak; green box, differential peak.

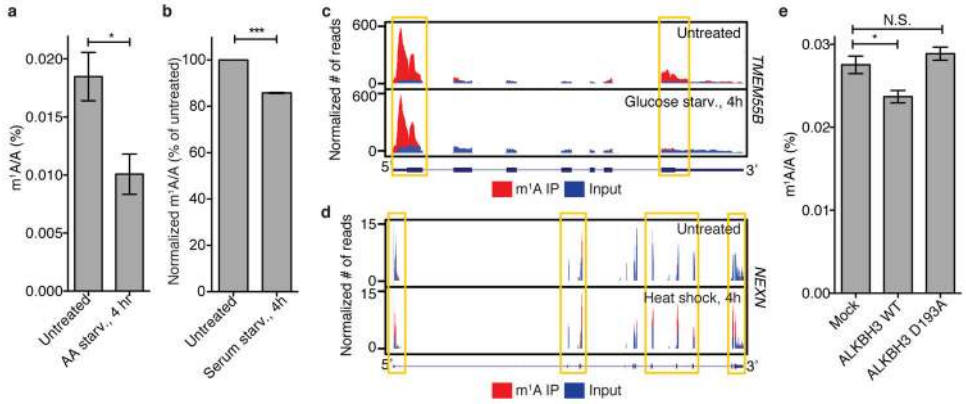

Extended Data Figure 9. m^{1}A in mRNA is a dynamic modification

a, **b**, LC-MS/MS quantification of m^{1}A in mRNA of untreated and amino acid (AA)-starved (**a**) or serum-starved (**b**) HepG2. Mean values ± s.e.m. are shown, $n = 3$, $*P \leq 0.05$, $***P \leq 0.001$, unpaired *t*-test. **c**, **d**, Representative plots of differentially methylated transcripts in untreated and glucose-starved (**c**) or heat shock-treated (**d**) HepG2 cells. Plot formats as in Fig. 2a. **e**, LC-MS/MS quantification of m^{1}A in mRNA of 293F cells overexpressing WT FLAG-ALKBH3 or an inactive mutant (D193A), presented as percentage of unmodified A. Mean values ±s.e.m. are shown, $n = 3$, $*P \leq 0.05$, NS, $P > 0.05$, one-way ANOVA with Dunnet's multiple comparison test.

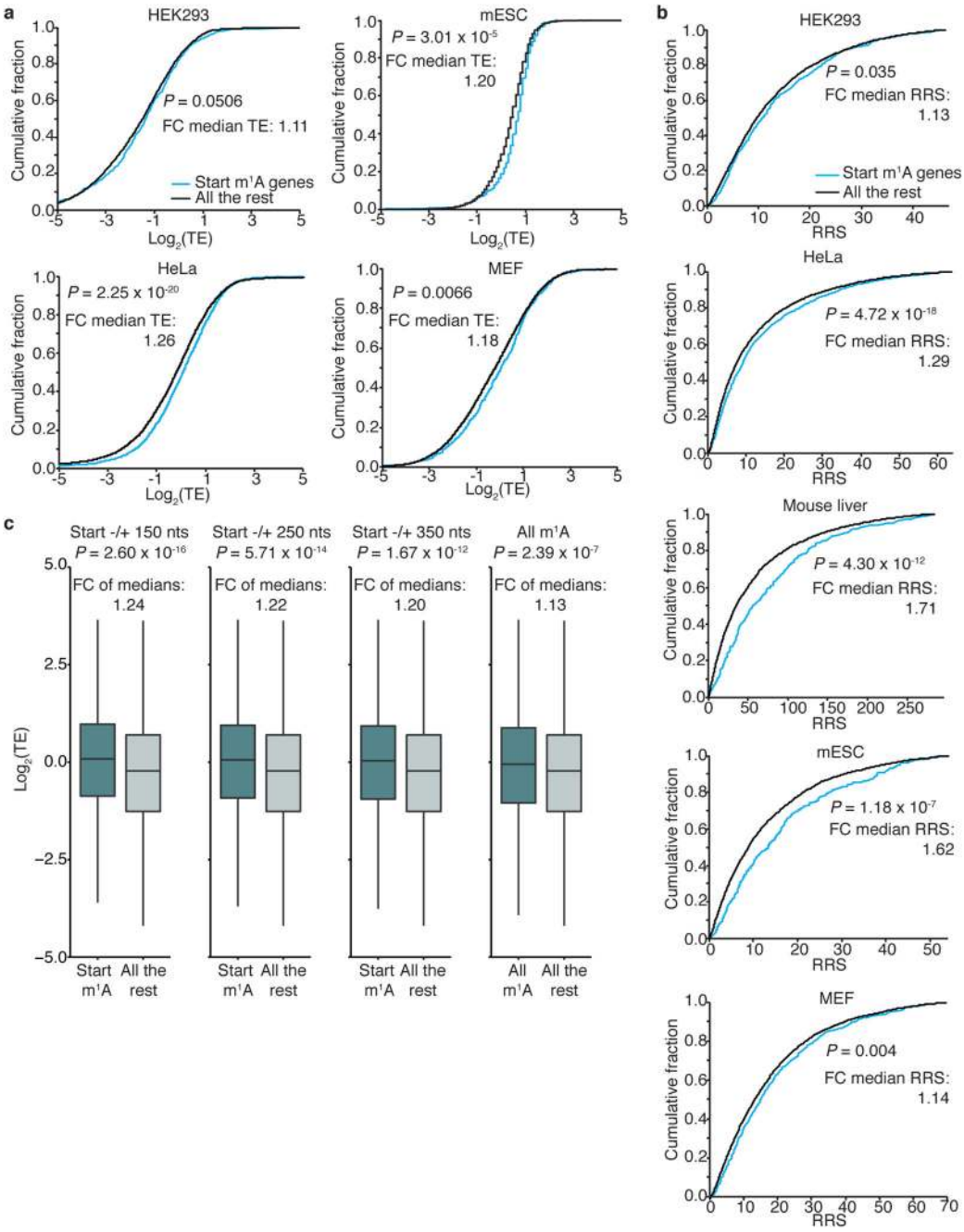

Extended Data Figure 10. m^{1}A around the start codon correlates with higher translation efficiency (TE)

a, Cumulative distribution of $\log_2$(TE) in genes methylated in a 300-nucleotide window centred on the start codon compared to all other genes, in the indicated human and mouse cell types. *P* values (*t*-test) and fold-changes (FC) of median TE values (Start m^{1}A genes/All the rest) are indicated. **b**, Genes methylated in a 300-nucleotide window centred on the AUG start codon have a higher ribosome release score (RRS = TE[CDS]/TE[3′ UTR]) compared to all other genes in the indicated cell types. RRSs, which are 'normalized' to ribosomal drop-off in the 3′ UTR, are in line with TE scores. *P* values (Mann–Whitney *U* test) and

fold-changes (FC) of median RRS values (Start m^1A genes/All the rest) are indicated. **c**, Genes methylated in different start codon window sizes have higher TE compared to all other genes, in HeLa cells. When considering all m^1A genes, including those methylated outside the start codon window, the effect is reduced. *P* values (*t*-test) and fold-changes (FC) of median TE values (Start m^1A genes/All the rest) are indicated. Box limits represent 25th percentile, median and 75th percentile; whiskers extend from the limit to the highest and lowest value within 1.5 IQR (interquartile range).

Supplementary Material

Refer to Web version on PubMed Central for supplementary material.

Acknowledgments

The work was supported by the National Institutes of Health HG008688 and GM71440 grants to C.H., GM113194 grant to T.P. and C.H. and grants from the Flight Attendant Medical Research Institute (FAMRI), Israel Science Foundation (ISF grant no. 1667/12), Israeli Centers of Excellence (I-CORE) Program (ISF grants no. 41/11 and no. 1796/12), Ernest and Bonnie Beutler Research Program and Kahn Family Foundation to G.R. A part of this work was funded by the Chicago Biomedical Consortium with support from the Searle Funds at The Chicago Community Trust (to D.D. and C.H.). C.H. is an investigator of the Howard Hughes Medical Institute (HHMI). G.R. is a member of the Sagol Neuroscience Network and holds the Djerassi Chair for Oncology at the Sackler Faculty of Medicine, Tel-Aviv University, Israel. D.D. is supported by a Human Frontier Science Program (HFSP) long-term fellowship. S.N. is an HHMI Fellow of the Damon Runyon Cancer Research Foundation (DRG-2215-15), previously supported by a Yen post-doctoral fellowship in interdisciplinary research. Q.D. is supported by the National Institutes of Health grant HG006699. We wish to thank S. Farage-Barhom, K. Cesarkas and E. Glick-Saar for help with deep sequencing.

References

1. Dominissini D, et al. Topology of the human and mouse m6A RNA methylomes revealed by m6A-seq. Nature. 2012; 485:201–206. [PubMed: 22575960]
2. Meyer KD, et al. Comprehensive analysis of mRNA methylation reveals enrichment in 3′ UTRs and near stop codons. Cell. 2012; 149:1635–1646. [PubMed: 22608085]
3. Carlile TM, et al. Pseudouridine profiling reveals regulated mRNA pseudouridylation in yeast and human cells. Nature. 2014; 515:143–146. [PubMed: 25192136]
4. Schwartz S, et al. Transcriptome-wide mapping reveals widespread dynamic-regulated pseudouridylation of ncRNA and mRNA. Cell. 2014; 159:148–162. [PubMed: 25219674]
5. Li X, et al. Chemical pulldown reveals dynamic pseudouridylation of the mammalian transcriptome. Nature Chem Biol. 2015; 11:592–597. [PubMed: 26075521]
6. Squires JE, et al. Widespread occurrence of 5-methylcytosine in human coding and non-coding RNA. Nucleic Acids Res. 2012; 40:5023–5033. [PubMed: 22344696]
7. Khoddami V, Cairns BR. Identification of direct targets and modified bases of RNA cytosine methyltransferases. Nature Biotechnol. 2013; 31:458–464. [PubMed: 23604283]
8. Fu Y, Dominissini D, Rechavi G, He C. Gene expression regulation mediated through reversible m^6A RNA methylation. Nature Rev Genet. 2014; 15:293–306. [PubMed: 24662220]
9. Li S, Mason CE. The pivotal regulatory landscape of RNA modifications. Annu Rev Genomics Hum Genet. 2014; 15:127–150. [PubMed: 24898039]
10. Machnicka MA, et al. MODOMICS: a database of RNA modification pathways—2013 update. Nucleic Acids Res. 2013; 41:D262–D267. [PubMed: 23118484]
11. Dunn DB. The occurrence of 1-methyladenine in ribonucleic acid. Biochim Biophys Acta. 1961; 46:198–200. [PubMed: 13725042]
12. Hall RH. Method for isolation of 2′-O-methylribonucleotides and N1-methyladenosine from ribonucleic acid. Biochim Biophys Acta. 1963; 68:278–283.

13. El Yacoubi B, Bailly M, de Crécy-Lagard V. Biosynthesis and function of posttranscriptional modifications of transfer RNAs. Annu Rev Genet. 2012; 46:69–95. [PubMed: 22905870]
14. Sharma S, Watzinger P, Kötter P, Entian KD. Identification of a novel methyltransferase, Bmt2, responsible for the *N*-1-methyl-adenosine base modification of 25S rRNA in *Saccharomyces cerevisiae*. Nucleic Acids Res. 2013; 41:5428–5443. [PubMed: 23558746]
15. Anderson, JT.; Droogmans, L. Fine-Tuning of RNA Functions by Modification and Editing. Grosjean, H., editor. Vol. 12. 2005. p. 121-139.
16. Macon JB, Wolfenden R. 1-Methyladenosine. Dimroth rearrangement and reversible reduction. Biochemistry. 1968; 7:3453–3458. [PubMed: 5681457]
17. Desrosiers R, Friderici K, Rottman F. Identification of methylated nucleosides in messenger RNA from Novikoff hepatoma cells. Proc Natl Acad Sci USA. 1974; 71:3971–3975. [PubMed: 4372599]
18. Zhang Y, et al. Model-based analysis of ChIP-Seq (MACS). Genome Biol. 2008; 9:R137. [PubMed: 18798982]
19. Ingolia NT, Lareau LF, Weissman JS. Ribosome profiling of mouse embryonic stem cells reveals the complexity and dynamics of mammalian proteomes. Cell. 2011; 147:789–802. [PubMed: 22056041]
20. Lee S, et al. Global mapping of translation initiation sites in mammalian cells at single-nucleotide resolution. Proc Natl Acad Sci USA. 2012; 109:E2424–E2432. [PubMed: 22927429]
21. Gao X, et al. Quantitative profiling of initiating ribosomes *in vivo*. Nature Methods. 2015; 12:147–153. [PubMed: 25486063]
22. Takuma H, et al. Substrate tRNA recognition mechanism of eubacterial tRNA (m1A58) methyltransferase (TrmI). J Biol Chem. 2015; 290:5912–5925. [PubMed: 25593312]
23. Ozanick S, Krecic A, Andersland J, Anderson JT. The bipartite structure of the tRNA m1A58 methyltransferase from *S. cerevisiae* is conserved in humans. RNA. 2005; 11:1281–1290. [PubMed: 16043508]
24. Kozak M. Regulation of translation via mRNA structure in prokaryotes and eukaryotes. Gene. 2005; 361:13–37. [PubMed: 16213112]
25. Clancy MJ, Shambaugh ME, Timpte CS, Bokar JA. Induction of sporulation in *Saccharomyces cerevisiae* leads to the formation of N6-methyladenosine in mRNA: a potential mechanism for the activity of the IME4 gene. Nucleic Acids Res. 2002; 30:4509–4518. [PubMed: 12384598]
26. Schwartz S, et al. High-resolution mapping reveals a conserved, widespread, dynamic mRNA methylation program in yeast meiosis. Cell. 2013; 155:1409–1421. [PubMed: 24269006]
27. Peifer C, et al. Yeast Rrp8p, a novel methyltransferase responsible for m^1A 645 base modification of 25S rRNA. Nucleic Acids Res. 2013; 41:1151–1163. [PubMed: 23180764]
28. Jia G, et al. N6-methyladenosine in nuclear RNA is a major substrate of the obesity-associated FTO. Nature Chem Biol. 2011; 7:885–887. [PubMed: 22002720]
29. Aas PA, et al. Human and bacterial oxidative demethylases repair alkylation damage in both RNA and DNA. Nature. 2003; 421:859–863. [PubMed: 12594517]
30. Ougland R, et al. AlkB restores the biological function of mRNA and tRNA inactivated by chemical methylation. Mol Cell. 2004; 16:107–116. [PubMed: 15469826]
31. Zur H, Tuller T. New universal rules of eukaryotic translation initiation fidelity. PLOS Comput Biol. 2013; 9:e1003136. [PubMed: 23874179]
32. Parsyan A, et al. mRNA helicases: the tacticians of translational control. Nature Rev Mol Cell Biol. 2011; 12:235–245. [PubMed: 21427765]
33. Helm M, Giegé R, Florentz C. A Watson-Crick base-pair-disrupting methyl group (m1A9) is sufficient for cloverleaf folding of human mitochondrial tRNALys. Biochemistry. 1999; 38:13338–13346. [PubMed: 10529209]
34. Guttman M, Russell P, Ingolia NT, Weissman JS, Lander ES. Ribosome profiling provides evidence that large noncoding RNAs do not encode proteins. Cell. 2013; 154:240–251. [PubMed: 23810193]

35. Lu L, Yi C, Jian X, Zheng G, He C. Structure determination of DNA methylation lesions N^1-meA and N^3-meC in duplex DNA using a cross-linked protein-DNA system. Nucleic Acids Res. 2010; 38:4415–4425. [PubMed: 20223766]
36. He C, et al. A methylation-dependent electrostatic switch controls DNA repair and transcriptional activation by *E. coli* Ada. Mol Cell. 2005; 20:117–129. [PubMed: 16209950]
37. Harcourt EM, Ehrenschwender T, Batista PJ, Chang HY, Kool ET. Identification of a selective polymerase enables detection of N^6-methyladenosine in RNA. J Am Chem Soc. 2013; 135:19079–19082. [PubMed: 24328136]
38. Sonenberg N, Hinnebusch AG. Regulation of translation initiation in eukaryotes: mechanisms and biological targets. Cell. 2009; 136:731–745. [PubMed: 19239892]
39. Wang X, et al. N^6-methyladenosine modulates messenger RNA translation efficiency. Cell. 2015; 161:1388–1399. [PubMed: 26046440]
40. Kierzek E, Kierzek R. The thermodynamic stability of RNA duplexes and hairpins containing N^6-alkyladenosines and 2-methylthio-N^6-alkyladenosines. Nucleic Acids Res. 2003; 31:4472–4480. [PubMed: 12888507]
41. Roost C, et al. Structure and thermodynamics of N^6-methyladenosine in RNA: a spring-loaded base modification. J Am Chem Soc. 2015; 137:2107–2115. [PubMed: 25611135]
42. Li, X., et al. Transcriptome-wide mapping reveals reversible and dynamic N^1-methyladenosine methylome. Nat Chem Biol. 2016. http://dx.doi.org/10.1038/nchembio.2040
43. Geula S, et al. m^6A mRNA methylation facilitates resolution of naïve pluripotency toward differentiation. Science. 2015; 347:1002–1006. [PubMed: 25569111]
44. Wang X, et al. N^6-methyladenosine-dependent regulation of messenger RNA stability. Nature. 2014; 505:117–120. [PubMed: 24284625]
45. Hienzsch A, Deiml C, Reiter V, Carell T. Total synthesis of the hypermodified RNA bases wybutosine and hydroxywybutosine and their quantification together with other modified RNA bases in plant materials. Chemistry. 2013; 19:4244–4248. [PubMed: 23417961]
46. Pearson D, et al. LC-MS based quantification of 2′-ribosylated nucleosides Ar(p) and Gr(p) in tRNA. Chem Commun (Camb). 2011; 47:5196–5198. [PubMed: 21448475]
47. Hauenschild R, et al. The reverse transcription signature of N-1-methyladenosine in RNA-Seq is sequence dependent. Nucleic Acids Res. 2015; 43:9950–9964.10.1093/nar/gkv895 [PubMed: 26365242]
48. Jones JW, Robins RK. Purine Nucleosides. III. Methylation studies of certain naturally occurring purine nucleosides. J Am Chem Soc. 1963; 85:193–201.
49. Dai Q, et al. Identification of recognition residues for ligation-based detection and quantitation of pseudouridine and N^6-methyladenosine. Nucleic Acids Res. 2007; 35:6322–6329. [PubMed: 17881375]
50. Hobartner C, et al. The synthesis of 2′-*O*-[(triisopropylsilyl)oxy] methyl (*TOM*) phosphoramidites of methylated ribonucleosides (m^1G, m^2G, $m^2{}_2G$, m^1I, m^3U, m^4C, m^6A, $m^2{}_6A$) for use in automated RNA solid-phase synthesis. Monatsh Chem. 2003; 134:851–873.
51. Dominissini D, Moshitch-Moshkovitz S, Salmon-Divon M, Amariglio N, Rechavi G. Transcriptome-wide mapping of N^6-methyladenosine by m^6A-seq based on immunocapturing and massively parallel sequencing. Nature Protocols. 2013; 8:176–189. [PubMed: 23288318]
52. Langmead B, Salzberg SL. Fast gapped-read alignment with Bowtie 2. Nature Methods. 2012; 9:357–359. [PubMed: 22388286]
53. Li H, et al. The Sequence Alignment/Map format and SAMtools. Bioinformatics. 2009; 25:2078–2079. [PubMed: 19505943]
54. Anders S, Pyl PT, Huber W. HTSeq—a Python framework to work with high-throughput sequencing data. Bioinformatics. 2015; 31:166–169. [PubMed: 25260700]
55. Robinson MD, McCarthy DJ, Smyth GK. edgeR: a Bioconductor package for differential expression analysis of digital gene expression data. Bioinformatics. 2010; 26:139–140. [PubMed: 19910308]
56. Trapnell C, et al. Transcript assembly and quantification by RNA-Seq reveals unannotated transcripts and isoform switching during cell differentiation. Nature Biotechnol. 2010; 28:511–515. [PubMed: 20436464]

57. Martin M. Cutadapt removes adapter sequences from high-throughput sequencing reads. EMBnet journal. 2011; 17:10–12.
58. Kim D, et al. TopHat2: accurate alignment of transcriptomes in the presence of insertions, deletions and gene fusions. Genome Biol. 2013; 14:R36. [PubMed: 23618408]
59. Salmon-Divon M, Dvinge H, Tammoja K, Bertone P. PeakAnalyzer: genome-wide annotation of chromatin binding and modification loci. BMC Bioinformatics. 2010; 11:415. [PubMed: 20691053]
60. Quinlan AR, Hall IM. BEDTools: a flexible suite of utilities for comparing genomic features. Bioinformatics. 2010; 26:841–842. [PubMed: 20110278]
61. Lorenz R, et al. ViennaRNA Package 2.0. Algorithms Mol Biol. 2011; 6:26. [PubMed: 22115189]
62. Trotta E. On the normalization of the minimum free energy of RNAs by sequence length. PLoS One. 2014; 9:e113380. [PubMed: 25405875]
63. Wan Y, Qu K, Ouyang Z, Chang HY. Genome-wide mapping of RNA structure using nuclease digestion and high-throughput sequencing. Nature Protocols. 2013; 8:849–869. [PubMed: 23558785]
64. Kertesz M, et al. Genome-wide measurement of RNA secondary structure in yeast. Nature. 2010; 467:103–107. [PubMed: 20811459]
65. Heinz S, et al. Simple combinations of lineage-determining transcription factors prime cis-regulatory elements required for macrophage and B cell identities. Mol Cell. 2010; 38:576–589. [PubMed: 20513432]
66. Bailey TL, Elkan C. Fitting a mixture model by expectation maximization to discover motifs in biopolymers. Proc Int Conf Intell Syst Mol Biol. 1994; 2:28–36. [PubMed: 7584402]
67. Crooks GE, Hon G, Chandonia JM, Brenner SE. WebLogo: a sequence logo generator. Genome Res. 2004; 14:1188–1190. [PubMed: 15173120]
68. Linder B, et al. Single-nucleotide-resolution mapping of m^6A and m^6Am throughout the transcriptome. Nature Methods. 2015; 12:767–772. [PubMed: 26121403]
69. Hinrichs AS, et al. The UCSC Genome Browser Database: update 2006. Nucleic Acids Res. 2006; 34:D590–D598. [PubMed: 16381938]
70. Geiger, T.; Wehner, A.; Schaab, C.; Cox, J.; Mann, M. Comparative proteomic analysis of eleven common cell lines reveals ubiquitous but varying expression of most proteins. Mol Cell Proteomics. 2012. http://dx.doi.org/10.1074/mcp.M111.014050
71. Graumann J, et al. Stable isotope labeling by amino acids in cell culture (SILAC) and proteome quantitation of mouse embryonic stem cells to a depth of 5,111 proteins. Mol Cell Proteomics. 2008; 7:672–683. [PubMed: 18045802]
72. Schwanhäusser B, et al. Global quantification of mammalian gene expression control. Nature. 2011; 473:337–342. [PubMed: 21593866]
73. Li JJ, Bickel PJ, Biggin MD. System wide analyses have underestimated protein abundances and the importance of transcription in mammals. PeerJ. 2014; 2:e270. [PubMed: 24688849]
74. Noderer WL, et al. Quantitative analysis of mammalian translation initiation sites by FACS-seq. Mol Syst Biol. 2014; 10:748. [PubMed: 25170020]
75. Huppert JL, Bugaut A, Kumari S, Balasubramanian S. G-quadruplexes: the beginning and end of UTRs. Nucleic Acids Res. 2008; 36:6260–6268. [PubMed: 18832370]
76. Beaudoin JD, Perreault JP. 5′-UTR G-quadruplex structures acting as translational repressors. Nucleic Acids Res. 2010; 38:7022–7036. [PubMed: 20571090]
77. Lewis BP, Burge CB, Bartel DP. Conserved seed pairing, often flanked by adenosines, indicates that thousands of human genes are microRNA targets. Cell. 2005; 120:15–20. [PubMed: 15652477]

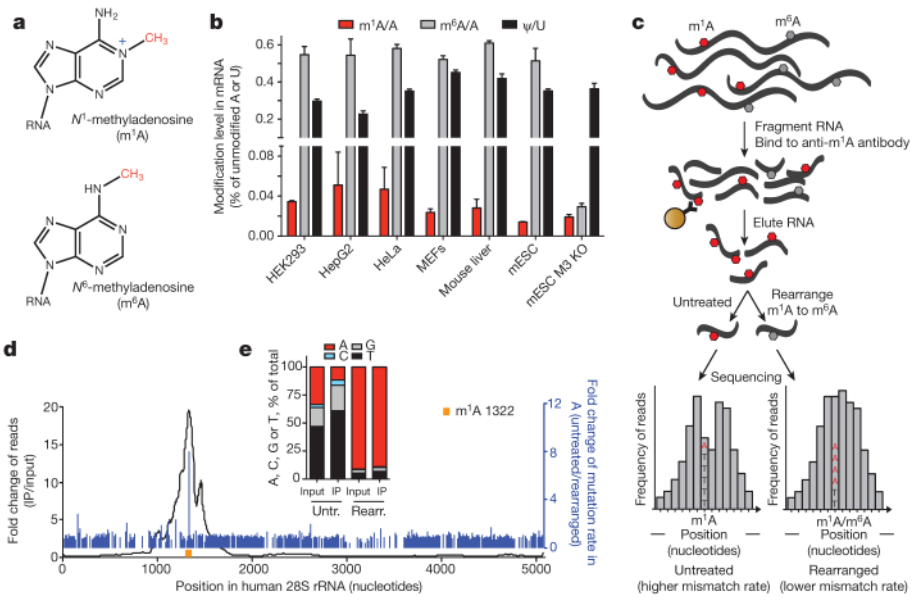

Figure 1. Development of m^{1}A-seq to map a newly identified constituent of mammalian mRNA

a, Chemical structures of m^{1}A and m^{1}A is in blue. **b**, LC-MS/MS quantitation of m^{1}A, m^{6}A and Ψ in human and mouse mRNA isolated from the indicated cell types. The level of each modified nucleoside is indicated as a percentage of the unmodified one. Mean values ± s.e.m. are shown, $n = 3$. MEFs, mouse embryonic fibroblasts; mESC, mouse embryonic stem cells; M3 KO, *Mettl3* knockout. **c**, Schematic outline of m^{1}A-seq. RNA is fragmented and subjected to immunoprecipitation using anti-m^{1}A antibody. Eluted RNA fragments are converted to cDNA and sequenced, or treated to induce partial m^{1}A-to-m^{6}A rearrangement before cDNA synthesis. m^{1}A causes both reverse transcription stops and read-throughs accompanied by mismatches, to produce typical peaks with a central trough and an adenosine with increased mismatch rate (left). Partial rearrangement of m^{1}A to m^{6}A attenuates the effect (right). m^{1}A is in red, m^{6}A is in grey; mismatch rate is illustrated as the ratio between A (red) and T (black). **d**, Detection of the known m^{1}A 1322 site (yellow) in human 28S rRNA validates m^{1}A-seq (black curve). High fold-change in mismatch rate (before and after m^{1}A-to-m^{6}A rearrangement in immunoprecipitation, blue lines) independently identifies m^{1}A 1322 with single-nucleotide resolution. **e**, Mismatch rates in m^{1}A 1322 increase after immunoprecipitation and decrease upon rearrangement.

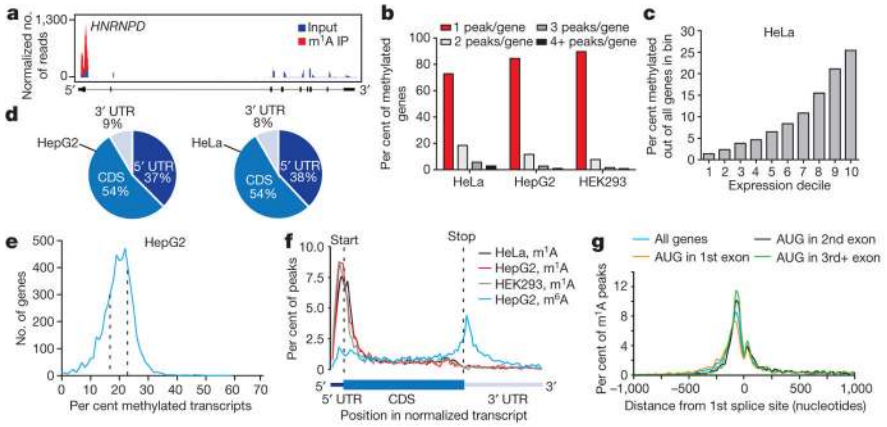

Figure 2. m^{1}A is associated with translation initiation sites (TISs) in the human transcriptome

a, Representative plot of a methylated transcript. Normalized sequence coverage of immunoprecipitation (m^{1}A IP, red) and input (blue) are indicated above the gene architecture in UCSC format. Thin black boxes represent the 5′ and 3′ untranslated regions (UTRs), thick black boxes represent the coding sequences (CDS) and thin lines represent introns. **b**, The percentage of methylated genes that carry 1, 2, 3 or 4+ peaks per gene in the indicated human cell types. Most methylated genes carry only one m^{1}A peak. **c**, The percentage of methylated genes in HeLa cells increases with expression level. **d**, Pie charts presenting the fraction of m^{1}A peaks in each of three non-overlapping transcript segments (5′ UTR, CDS and 3′ UTR) in the indicated human cell types. **e**, Stoichiometry (fraction) of methylated transcripts in genes that carry one m^{1}A peak in HepG2 mRNA. Plotted is the number of genes sorted by percentage of methylated transcripts. Dashed lines define the stoichiometry interquartile range (17–23%). **f**, Metagene profiles of m^{1}A peak distribution along a normalized transcript composed of three rescaled non-overlapping segments illustrated below, in the indicated human cell types. m^{1}A peaks cluster around the AUG start codon. For comparison, the distribution of m^{6}A peaks in HepG2 is superimposed. **g**, Metagene profiles of m^{1}A peak distribution in a non-normalized window centred on the first splice site. Peaks are sorted by the exon containing the AUG codon in that gene.

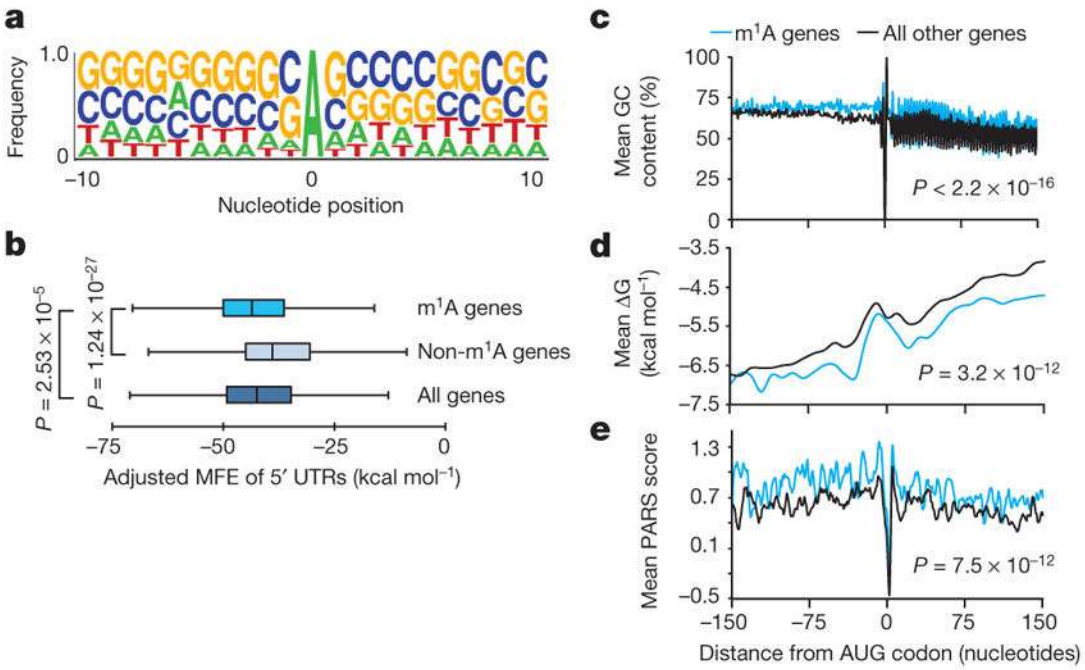

Figure 3. m^{1}A occurs in GC-rich sequence contexts and in genes with structured 5′ UTRs

a, Sequence frequency logo for a set of 192 adenosines in peak areas that have a higher mismatch rate in immunoprecipitation relative to input (FC ≥6) in HepG2 demonstrates the GC-rich context of m^{1}A. **b**, Length-adjusted minimum free energy (aMFE) for 5′ UTRs of methylated, unmethylated and all genes. Box limits represent 25th percentile, median and 75th percentile, whiskers represent 2.5 and 97.5 percentiles. *P* values are indicated, *t*-test. Analysis was based on human common peaks (see Methods). **c**–**e**, A sliding window of mean GC content (**c**), ΔG (**d**) and PARS scores (**e**) in a ±150-nucleotide window centred on the AUG start codon of methylated genes compared to all the rest, in HepG2 cells. *P* values are indicated; Kolmogorov–Smirnov test, *t*-test and Kolmogorov–Smirnov test, respectively.

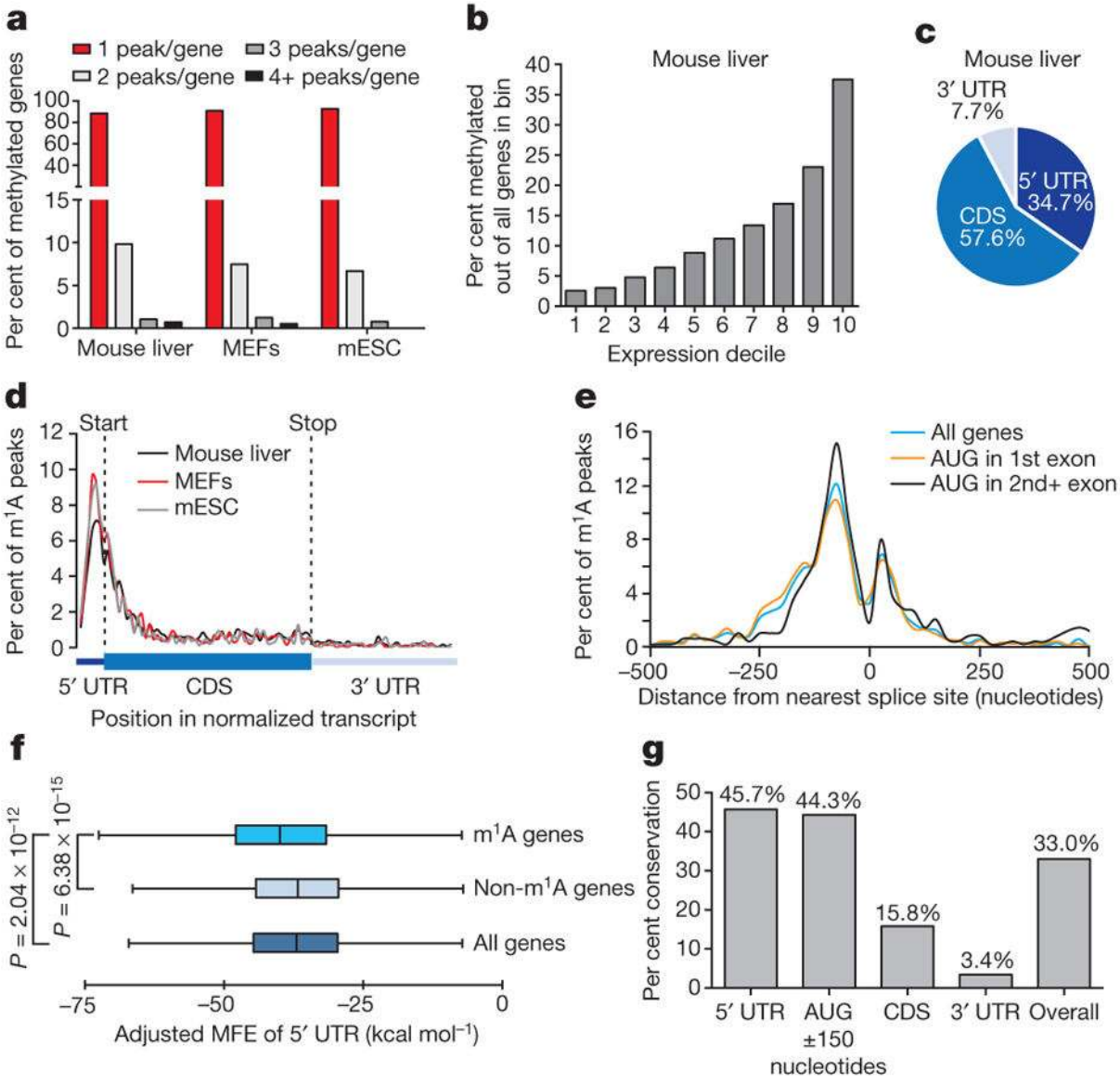

Figure 4. m^{1}A methylome conservation between human and mouse

a, The percentage of methylated genes that carry 1, 2, 3 or 4+ peaks per gene in the indicated mouse cell types. Most genes carry only one m^{1}A peak. **b**, The percentage of methylated genes in mouse liver cells increases with expression level. **c**, Pie chart presenting the fraction of m^{1}A peaks in each of three non-overlapping transcript segments (5′ UTR, CDS and 3′ UTR) in mouse liver. **d**, Metagene profiles of m^{1}A peak distribution along a normalized transcript composed of three rescaled non-overlapping segments illustrated below, in the indicated mouse cell types. m^{1}A peaks cluster around the AUG start codon. **e**, Metagene profiles of mouse m^{1}A peak distribution in a non-normalized window centred on the nearest splice site. Peaks are sorted by the exon containing the AUG codon in that gene. **f**, Length-adjusted minimum free energy (aMFE) for 5′ UTRs of methylated, unmethylated and all genes in mouse liver. Box limits and whiskers are as indicated in Fig. 3b. *P* values are

indicated, *t*-test. **g**, Human–mouse m^1A conservation expressed as per cent of orthologous positions with shared m^1A peaks according to their location in the transcript.

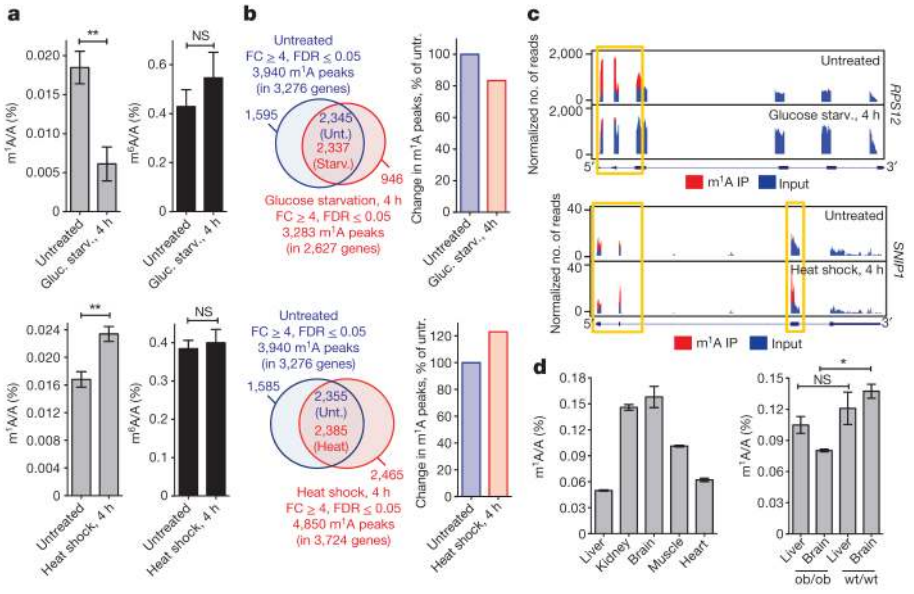

Figure 5. m^{1}A in mRNA is a dynamic modification that responds to changing physiological and stress conditions, and varies between tissues

a, LC-MS/MS quantification of m^{1}A (left, grey) and m^{6}A (right, black) in mRNA of untreated and glucose-starved (upper panels) or heat shock-treated (lower panels) HepG2 cells, presented as percentage of unmodified A. Mean values ± s.e.m. are shown, $n = 3$, $^{**}P \leq 0.01$, not significant (NS) $P > 0.05$, unpaired t-test. **b**, Venn diagrams of differential and shared m^{1}A peaks in untreated and glucose-starved (left upper panel) or heat shock-treated (left lower panel) HepG2 cells. The overall change in the number of identified m^{1}A peaks is presented as per cent of untreated (right upper and lower panels). **c**, Representative plots of differentially methylated transcripts in untreated and glucose starved (upper panel) or heat-shock-treated (lower panel) HepG2 cells. Plot format as in Fig. 2a. Yellow boxes frame differential peaks. **d**, LC-MS/MS quantification of m^{1}A in the indicated wt/wt and ob/ob mouse tissues, presented as percentage of unmodified A. Mean values ± s.e.m. are shown, $n = 3$, $^{*}P \leq 0.05$, NS, $P > 0.05$, one-way ANOVA.

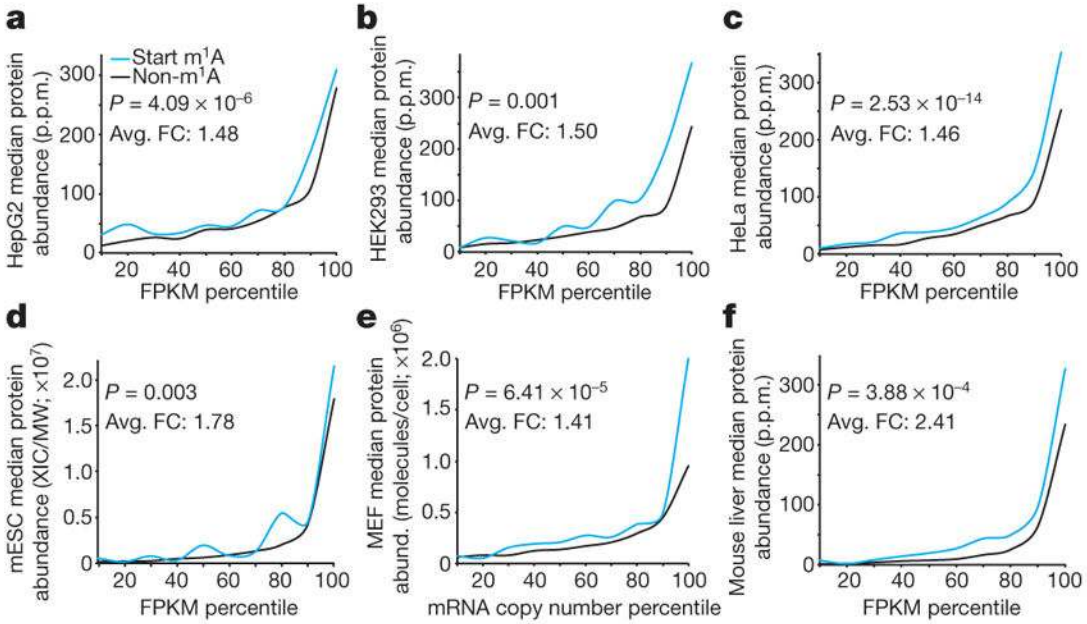

Figure 6. m^{1}A around the start codon correlates with higher protein levels

a–**f**, Genes methylated in a 300-nucleotide window centred on the start codon have higher protein levels than all other genes with similar RNA expression levels in HepG2 (**a**), HEK293 (**b**), HeLa (**c**), mESC (**d**), MEFs (**e**) and mouse liver (**f**). ANOVA m^{1}A *P* values against $\log_2$ protein levels and the average fold-change (Avg. FC) of median protein levels across all gene expression bins (Start m^{1}A/Non-m^{1}A) are indicated. FPKM, fragments per kilobase of transcript per million mapped reads.